Chapter 10 – NUMERICAL SOLUTIONS FOR THE CAWAPI CONFIGURATION ON UNSTRUCTURED GRIDS AT KTH/FOI, SWEDEN – PART I

By
Stefan Görtz and Adam Jirásek

10.1 SUMMARY

Steady and unsteady viscous simulations of a full-scale, semi-span and full-span model of the F-16XL-1 aircraft at seven different flight Reynolds/Mach number combinations have been performed with an unstructured CFD code. The steady-state simulations are with several turbulence models of different complexity. Detached-Eddy Simulation (DES) has been used to compute the unsteady flow. The computed results are compared with public domain flight-test data. Very good agreement is demonstrated for surface pressure distribution, local skin friction and boundary velocity profiles. The different turbulence models performed almost equally well, except the Spalart-Allmaras model, which failed to predict the flow qualitatively and quantitatively. The Differential Reynolds Stress Model (DRSM) outperformed all other models when it comes to local span-wise skin friction. DES was superior over RANS modeling at the highest angle of attack, where the flow over the outer wing is separated and partly unsteady.

10.2 NOMENCLATURE

α	=	angle of attack
β	=	sideslip angle
b	=	wing span
c	=	cord length
c_f	=	friction coefficient
c_P	=	pressure coefficient
M_∞	=	freestream Mach number
v	=	velocity
BL	=	butt line
CAWAPI	=	Cranked Arrow Wing Aerodynamics Project International
FC	=	Flight Condition
FS	=	Fuselage station
RANS	=	Reynold-Averaged Navier-Stokes

10.3 DENOTATION OF TURBULENCE MODELS

EARSM	=	Explicit Algebraic Reynolds Stress Model based on standard k-ω model
EARSM + CC	=	EARSM based on standard k-ω model with curvature corrections

Hellsten EARSM	=	EARSM based on Hellsten k-ω model
Hellsten EARSM + CC	=	EARSM based on Hellsten k-ω model with curvature corrections
DRSM	=	Differential Reynolds Stress Model
DES	=	Detached Eddy Simulation
S − A	=	Spalart-Allmaras model

10.4 INTRODUCTION

Current requirements for military aircraft result in a need for a better understanding of aircraft characteristics before full-scale production. For this purpose new and existing computational fluid dynamics (CFD) codes have to be validated and their technology readiness level checked and/or increased for military aircraft - both manned and unmanned. The benefits resulting from validated CFD codes are a reduction of project risks, enhanced analysis of system performance prior to flight and the ability to analyze unexpected flight behavior.

Flight data for CFD code validation has been obtained on and off the surface of the F-16XL-1 aircraft at subsonic and transonic speeds as documented by Lamar [10.1]. This data is unique both in that it is for a high-performance fighter aircraft and it is publicly accessible on the internet [10.2]. Furthermore, the data is not subject to wind tunnel blockage-, scaling- or Reynolds-number effects. Comparison between numerical and experimental data can be done at flight Reynolds numbers as opposed to wind-tunnel Reynolds numbers, circumventing the problem of modeling transition.

Researchers from several countries, after learning of this high Reynolds number flight-test data set, expressed interest in validating their CFD codes against flight measurements of surface pressures and flow, boundary layer velocity profiles and skin friction obtained on this high-performance aircraft. As a result, they joined with American participants in one 'facet' of a NATO Research and Technology Organization (RTO) Applied Vehicle Technology (AVT) task group. This facet was named the "Cranked Arrow Wing Aerodynamics Project International" (CAWAPI). The aim was to develop and document the best practices for each code so as to raise its technology readiness level when applied to this class of aircraft. New CFD solutions were generated by the team members, among them KTH and FOI, and placed into a CAWAPI archiving system using common data standards to facilitate timely data access to other team members.

Previous computational investigations of the F-16XL-1 have been performed by Lamar [10.1, 10.3] and Lessard [10.4]. The former was a flight, wind-tunnel and CFD comparison at subsonic and transonic speeds using a structured flow solver (`CFL3D`) with wall functions, whereas the latter was a subsonic analysis of a 0.04-scale model using an unstructured Euler code.

The present paper documents the Swedish contributions to CAWAPI. We present wall-resolved viscous computations of the full-scale aircraft at flight Reynolds numbers using state-of-the-art numerical techniques and turbulence models. The goal is to improve the understanding and modeling of vortical flows and to identify weaknesses in the modeling process. The paper begins with a description of the aircraft and the associated flight test program, followed by a presentation of the numerical method and the grid used here. The main part discusses the computed results and compares them to flight-test data.

10.5 FLIGHT CONDITIONS

Seven of the 99 CAWAP flight conditions (FC) [10.1] were selected for computation in CAWAPI. They represent different Reynolds/Mach number combinations at subsonic and transonic speeds, with and without sideslip. All seven flight conditions are listed with their nominal and actual values in Table 10-1.

Flight conditions 7, 19, and 46 are medium angle-of-attack vortical flow conditions at various subsonic Mach

Table 10-1: Flight Conditions (FC) to be Examined (Nominal Altitude, actual Mach Number, actual Angle of Attack, actual Side-Slip Angle, actual Reynolds Number).

FC	alt. [ft]	M_∞	α [°]	β [°]	Re
Minimum Flight Conditions to be examined:					
FC07	5,000	0.304	11.89	-0.133	44.40×10^6
FC19	10,000	0.360	11.85	+0.612	46.80×10^6
FC46	24,000	0.527	10.40	+0.684	46.90×10^6
FC70	22,300	0.970	4.37	+0.310	88.77×10^6
Additional Flight Conditions to be examined:					
FC25	10,000	0.242	19.84	+0.725	32.22×10^6
FC50	24,000	0.434	13.56	+5.310	39.41×10^6
FC51	24,000	0.441	12.89	-4.580	38.96×10^6

numbers and altitudes, whereas FC70 is a low angle of attack attached flow condition at a transonic Mach number of 0.97. Flight conditions 50 and 51 are also medium angle-of attack vortical flow conditions, but at sideslip angles of +5.31 and -4.58, respectively, and a mirrored full-span grid created from the standard grid was used. Flight condition 25 is at a high incidence angle and most interesting in terms of unsteady modeling.

All seven flight conditions were computed by KTH/FOI. Note that all calculations were made assuming fully turbulent flow. Flight conditions 7, 19, 25, 46 and 70 have zero nominal side slip and were computed as symmetric using the semi-span standard unstructured grid although the actual side-slip angles ranged from +0.725 to -0.133. For the full-span model simulations at FC50 and FC51 the actual angle of side slip was specified. The angle of attack was set to the actual angle of attack for all flight conditions.

10.6 AIRCRAFT DESCRIPTION AND GEOMETRY

The F-16XL-1 is a single-seat fighter-type prototype aircraft built by the General Dynamics Corporation (now a part of the Lockheed-Martin Aeronautics Company). The aircraft has been developed from a full-scale development F-16A airframe by stretching the fuselage and adding a cranked-arrow wing, a modified fuel system and a modified flight-control system. It has scheduled leading-edge flaps, elevon, and ailerons on the wing for control. Details on the construction of the aircraft, its flight testing and its intended mission are given in Ref. [10.5–10.8].

The design of the cranked-arrow wing was a cooperative effort of the NASA Langley Research Center and the General Dynamics Corporation. The results of various wind-tunnel investigations are reported in Ref. [10.9–10.11]. The new wing was designed to provide the F-16 aircraft with improved supersonic performance, whilst maintaining transonic performance comparable with that provided by the current F-16 design, thus giving the aircraft a greater operational range. The resulting design has a leading-edge sweep angle of 70° inboard and 50° outboard of the crank. To alleviate a pitch instability that occurred at high angles of attack in wind-tunnel tests an "S-blend curve" was placed in the leading edge at the juncture of the wing with the fuselage. The aircraft was most recently used in the "Cranked-Arrow Wing Aerodynamics Project" (CAWAP) to test boundary layer pressures and distribution. The project began as a part of the high-lift element of the NASA High-Speed Research Program, developing technologies applicable to the High-Speed Civil Transport. This required modifications to the aircraft, which are described in detail in Ref. [10.1] and [10.3], notably strips of tubing along the leading edge to the trailing edge of the wing to sense static pressure on the wing and obtain pressure distribution data. The instrumented aircraft is shown in flight in Fig. 10-1. The starboard-side wing received data on pressure

distribution and the port-side wing had three types of instrumentation: modified Preston tubes to measure local skin friction, boundary layer rakes to measure boundary layer profiles and hot films to determine boundary layer transition locations. Surface tufts, surface oil flow and surface liquid crystal transducer responses were recorded using a special video installation. The pressure and surface-flow data were used for the purpose of establishing the effect of variations in Mach number on the local flow. The first flight of the CAWAP aircraft occurred on November 21, 1995, and the test program ended in April 1996. The CAWAP flight tests reported in Ref. [10.1] were with the air dams – upper-surface fences mounted near the wing leading-edge crank – and wingtip missiles installed. A detailed description of the CAWAP and CAWAPI projects can be found in Ref. [10.5].

Figure 10-1: F-16XL-1 Instrumentation Suite, Port Wing: Dummy Missiles with Built-in Video Cameras, Tufts, Flow-Visualization Paint Scheme, Video Targets; Starboard Wing: Pressure Belts (NASA Photo, 1996).

10.6.1 Geometry Simplifications

A geometry file of the F-16XL in `IGES` format, which is subject to International Traffic in Arms Regulations (ITAR), was provided to NASA and other CAWAPI team members by the Lockheed-Martin Aeronautics Company. Geometrical consistency between the real aircraft, including wing-tip mounted missiles, air dams and tail, and the CAD/CFD model was demonstrated in Ref. [10.1]. The `IGES` file was examined at EADS and multiple surfaces were found embedded in the description. A single set of surfaces was selected which includes some refinements in the leading-edge region for grid resolution. Later at NASA, certain features were adjusted for structured grid work, such as between the nozzle and the trailing-edge flap, the trailing edge of the missile rail fairing onto the wing, the engine inlet, a ‘step’ or ‘plate’ on the upper surface, and the smoothing out of a step in the longitudinal progression of the nose-boom outer diameter.

10.7 COMPUTATIONAL METHOD

10.7.1 Description of the Edge CFD Solver

KTH and FOI joined forces and used Edge [10.12] for contributing to CAWAPI. `Edge` is a flow solver for unstructured hybrid grids of arbitrary elements. The code is a proprietary code of the Swedish Defence Research Agency (FOI) where it is being developed. It is sheared with other users, among them KTH, based on a license agreement. User development of Edge is shared with FOI.
The parallel flow solver is based on an edge-based formulation and uses a node-centered finite volume scheme to solve the compressible Reynolds-Averaged Navier-Stokes (RANS) equations. For steady flows, the equations

are integrated toward steady state with an explicit multi-stage Runge-Kutta scheme. To accelerate convergence, implicit residual smoothing and a multi-grid technique can be employed. Low Mach-number preconditioning is also available. The spatial discretization is either second order central or second order upwind.
Time-accurate calculations are done either by Runge-Kutta time marching with a global time step or by implicit time marching with explicit sub-iterations, so-called "dual time stepping" [10.13].
The adaptive mesh refinement (AMR) module allows for local h-refinement of the hybrid grid by cell subdivision based on a sensor derived from the flow solution. In addition, there are three sensors for identifying vortices. They are based on the total pressure ratio, the production of entropy and an eigenvalue analysis of the velocity gradient tensor, respectively [10.14, 10.15].

10.7.2 Turbulence Modeling in Edge

The `Edge` code contains several eddy-viscosity turbulence models based on the Boussinesq hypothesis as well as a suite of Explicit Algebraic Reynolds Stress Models (EARSM). It also contains a Differential Reynolds Stress Model (DRSM), an algebraic hybrid RANS-LES (Large-Eddy Simulation) model [10.16, 10.17], and Detached Eddy Simulation (DES) capability.

10.7.2.1 Spalart-Allmaras Model of Turbulence (S-A)

The Spalart-Allmaras model [10.18] is a one-equation eddy viscosity model which models the Reynolds stress tensor as

$$\tau_{ij} = 2\mu_T S_{ij} \tag{1}$$

The Spalart-Allmaras model is one of the frequently used models in aerodynamic CFD calculations. The model is denoted S-A in this article.

10.7.2.2 Explicit Algebraic Reynolds Stress Model (EARSM)

The EARSM is an approximation of a Reynolds stress transport model in the weak-equilibrium limit. It behaves reasonably well for non-equilibrium flows. The Reynolds stress tensor is related to the anisotropy tensor a_{ij} through both the strain-rate tensor S_{ij} and the tensor of rotation Ω_{ij}. This model has been shown to give improved results but at a computational effort that is comparable to that of linear two-equation models. The implementation in Edge is done according to Wallin and Johansson [10.19]. The model has been used in combination with two types of k-ω models - the standard k-ω [10.20] model and the Hellsten k-ω model [10.21]. They are denoted EARSM and Hellsten EARSM, respectively, in this article.

10.7.2.3 Curvature Corrected Explicit Algebraic Reynolds Stress Model (EARSM + CC)

The weak-equilibrium limit can be too strong an assumption for flows with streamline curvature where the convective derivatives in the expression $\frac{Da_{ij}}{Dt}$ cannot be considered zero. The assumption of weak equilibrium can instead be defined in a curvilinear system. The tensor of rotation Ω_{ij} is corrected by adding the following term [10.22]

$$\Omega^*_{ij} = \Omega_{ij} - \frac{\tau}{A_0}\Omega^{(r)} \tag{2}$$

where A_0 is a constant. In general, the curvature correction has shown some improvements compared to the standard EARSM. However, it imposes some numerical problems and degenerates the convergence rate in some cases. In Edge, the correction was applied to both EARSM models, the one based on the standard k-ω model,

and the one based on the Hellsten k-ω model. They are denoted EARSM + CC and Hellsten EARSM + CC in this article.

10.7.2.4 Differential Reynolds Stress Model (DRSM)

This model does not model the Reynolds stress tensor in an algebraic formulation. It rather models additional correction terms in the Reynolds stress transport equation, for example

$$k\left(\frac{Da_{ij}}{Dt} - \mathcal{D}_{ij}^{(a)}\right) = \left(\mathcal{P}_{ij} - \frac{\overline{u_i u_j}}{k}\mathcal{P}\right) - \left(\epsilon_{ij} - \frac{\overline{u_i u_j}}{k}\epsilon\right) + \Pi_{ij} \tag{3}$$

$$a_{ij} = \frac{\overline{u_i u_j}}{k} - \frac{2}{3}\delta_{ij} \tag{4}$$

The model requires modeling of additional terms such as the pressure strain-tensor Π_{ij} and the dissipation rate ϵ_{ij}. The DRSM implementation in Edge has been done according to Hanjalic [10.23]. The model is denoted DRSM in this article.

10.7.2.5 Detached-Eddy Simulation (DES)

RANS methods have demonstrated an ability to predict attached flows very well at a relatively low computational cost. Large-Eddy Simulation (LES) methods, on the other hand, have proved to compute accurately separated flow fields. Although the computational costs of LES of turbulent flows is significantly less than that of direct numerical simulation (DNS), it is still too expensive for engineering applications involving thin boundary layers near surfaces, since the resolution needed to capture these layers results in exorbitant demands on CPU power and memory.

Spalart *et al* [10.24] proposed a hybrid LES/RANS turbulence model based on the one-equation Spalart-Allmaras eddy viscosity model as an alternative to the rather limited capabilities of inexpensive RANS models and improved features of computationally expensive LES. This hybrid approach, also called Detached-Eddy Simulation (DES), employs the S-A RANS turbulence model to overcome the near-wall resolution problem. This robust approach is aimed at high-Reynolds-number separated flows, where it smoothly switches from RANS mode in the boundary layer to LES in the separated region, improving results noticeably over purely RANS modeling. This model has shown promising performance in simulation of massively separated flows, for example, the flow over delta wings and delta-wing configurations at high angle of attack.

In the DES approach, the length scale d in the destruction term of the Spalart-Allmaras model,

$$\underbrace{\frac{D\tilde{\nu}}{Dt}}_{\text{convection}} = \underbrace{c_{b1}\tilde{S}\tilde{\nu}}_{\text{production}} + \underbrace{\frac{1}{\sigma}[\nabla\cdot((\nu+\tilde{\nu})\nabla\tilde{\nu}) + c_{b2}(\nabla\tilde{\nu})^2]}_{\text{diffusion}} - \underbrace{c_{w1}f_w\left(\frac{\tilde{\nu}}{d}\right)^2}_{\text{destruction}} \tag{5}$$

is modified so that the eddy viscosity crosses over from the usual Spalart-Allmaras RANS eddy viscosity near the wall to a proposed sub-grid scale (SGS) eddy viscosity, similar to that defined by Smagorinsky for SGS models, away from the wall. The Spalart-Allmaras wall destruction term, which reduces the turbulent viscosity in the laminar sub-layer, is proportional to $(\tilde{\nu}/d)^2$, where $\tilde{\nu}$ is the eddy viscosity and d the distance to the nearest wall. When this term is balanced with the production term, the eddy viscosity becomes proportional to $\hat{S}d^2$, where $\hat{S}$ is the local strain rate. The Smagorinski LES model, on the other hand, varies its sub-grid scale turbulent viscosity with the local strain rate and the grid spacing:

$$\nu \propto \hat{S}\Delta^2 \tag{6}$$

where $\Delta = \max(\Delta x, \Delta y, \Delta z)$. If d is replaced with Δ in the wall destruction term, the Spalart-Allmaras model will act similarly to the Smagorinski SGS model. Consequently, the DES formulation is obtained by replacing in the Spalart-Allmaras model the distance to the nearest wall, d, by $\tilde{d}$, where $\tilde{d}$ is defined as

$$\tilde{d} \equiv \min(d, C_{\text{DES}}\Delta) \tag{7}$$

Thus, the switch from RANS to LES depends on the spatial discretization. When the length scale d is smaller than the wall-parallel grid spacing Δ, which is typically the case for the highly stretched cells in the boundary layer, the model acts in RANS mode. When d is larger than Δ, the model acts in LES mode. This approach introduces only one additional model constant ($C_{\text{DES}} = 0.65$, calibrated from decaying isotropic turbulence) in the one-equation model of Spalart and Allmaras.
As `Edge` employs an edge-based formulation, where an edge connects two nodes, Δ is defined as the length of the largest edge of a cell,

$$\Delta = \max\left(\text{edge}_i\right) \tag{8}$$

or, on anisotropic grids, Δ can be based on the cell volume δV,

$$\Delta = (\delta V)^{1/3} \tag{9}$$

The DES implementation in `Edge` is described in more detail in Ref. [10.25, 10.26].
A powerful feature of DES is that it directly resolves turbulent eddies with increasing fidelity as the grid is refined [10.27]. Note that in RANS it is the mean flow that is computed – the role of grid refinement is to ensure convergence of the numerical solution and to minimize (or eliminate) the influence of the grid. In the fine-grid limit, the accuracy of RANS predictions are controlled by the turbulence model. In LES and DES, on the other hand, the role of grid refinement is resolution of additional physical features, i.e. a wider range of turbulent eddies are represented as grid spacings are decreased. Correspondingly, the contribution of the turbulence model to the solution decreases as the grid is refined. The fine-grid limit of DES (and LES) is a solution free of turbulence modeling errors, i.e. DNS. The model is denoted DES in the article.

10.7.3 Numerical Grid and Boundary Conditions

The standard unstructured grid used here was generated by NASA Langley Research Center using the grid generation packages `GridTool` [10.28] and `VGRIDns` [10.29]. It is described in detail elsewhere in this report. It is an all-tetrahedral viscous grid for the half-span, full-scale model of the F-16XL-1 (control surfaces not deflected) and is made up of 2,534,132 nodes, corresponding to 14,802,429 cells. The surface of the half-span model of the F-16XL was discretized with 160,266 triangular elements. The upper surface grid is shown in Fig. 10-2(a).

For the sake of completeness it must be pointed out that the grid generation approach followed by NASA is unconventional in that thin layers of right-angled tetrahedral cells are generated in the boundary layer region by the advancing-layers method (ALM). Unlike the conventional advancing-front method (AFM), which introduces cells in the field in a totally unstructured manner, the ALM generates layers of thin tetrahedral cells in a more orderly fashion while maintaining many advantageous features of the AFM. Outside the boundary layer a regular, nearly isotropic (inviscid) tetrahedral grid is generated by the AFM. The transition from thin layers to the regular grid is gradual and continuous because a common background grid is used to control both methods.

Note that for numerical reasons `Edge` requires the use of hybrid grids, where cell shapes that do not become skewed with stretching (e.g., hexahedral and prisms) are used in the viscous regions and tetrahedral cells away from viscous regions. To fulfill that requirement, the all-tetrahedral grid was converted into a hybrid

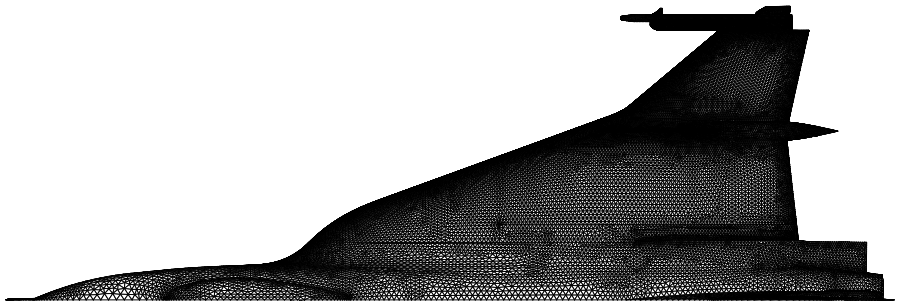

(a): **Unstructured surface grid for the F-16XL-1 half-span model (160,266 faces).**

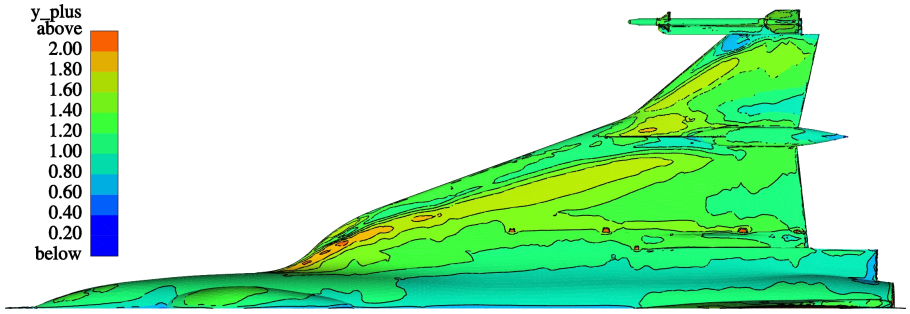

(b): **Levels of y^+ on the Upper Surface for FC19 (EARSM).**

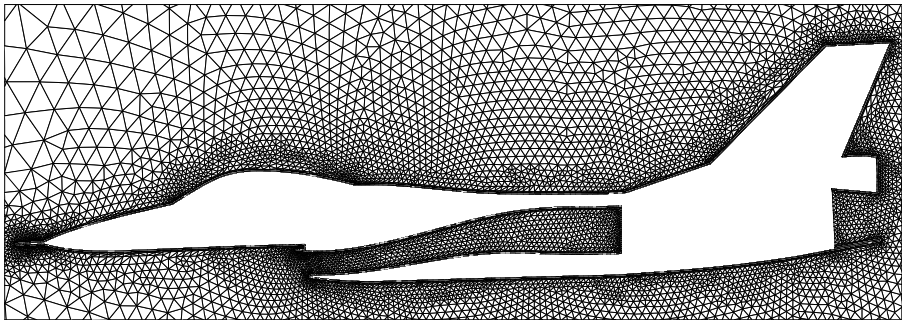

(c): **Symmetry plane of the hybrid grid showing the meshed inlet duct and nozzle.**

Figure 10-2: Computational Grid.

grid in `Cobalt` [10.30] format by combining the first nine layers of high-aspect-ratio, semi-structured tetrahedral cells off the aircraft surface into layers of prismatic cells using the commercial grid managements utility `Blacksmith` from Cobalt Solutions, LLC. This operation reduced the cell count to a total of 11,928,103, corresponding to 2,535,842 nodes. The program generated 9 layers of prismatic cells, corresponding to 1,442,394 prisms. The reason the grid has only 9 layers is that pyramids would be needed as "end caps" for layers that are not complete. Rather than adding another cell type it was decided to accepted 9 layers. It is important to note that the transition between the admittedly relatively few prismatic layers and the tetrahedral grid is very smooth, because there are a number of semi-structured ALM-generated viscous layers on top of the prismatic layers. The hybrid grid was used by the US Air Force Academy and KTH/FOI with `Cobalt` and `Edge`, respectively.

The resolution of the boundary layers requires the grid to be clustered in the direction normal to the surface with the spacing of the first grid point off the wall to be well within the laminar sublayer of the boundary layer. For turbulent flows, the first point off the wall should exhibit a y^+ value of less than 1.0. Here, the spacing of the first grid point normal to the solid wall is 5.0×10^{-6} m ($6.6 \times 10^{-7}c$). Away from the wall, the spacing increases by a ratio of 1.2. The resulting y^+ distribution over the upper surface of the aircraft model is shown for FC19 in Fig. (b). spacing normal to the numerical surface led to an average value of y^+ of less then one and a maximum y^+ of about two under the primary wing vortex, demonstrating that the grid is fine enough at the wall boundaries.

The engine duct is meshed all the way to the inlet duct exit plane. The nozzle is meshed from the engine mixing plane, see Fig. 10-2(c). The grid density off the aircraft surface is shown in Fig. 10-3, which depicts a wrinkly cutting plane through the grid at FS496 (fuselage station on airplane in inches, positive aft) , close to the trailing edge.

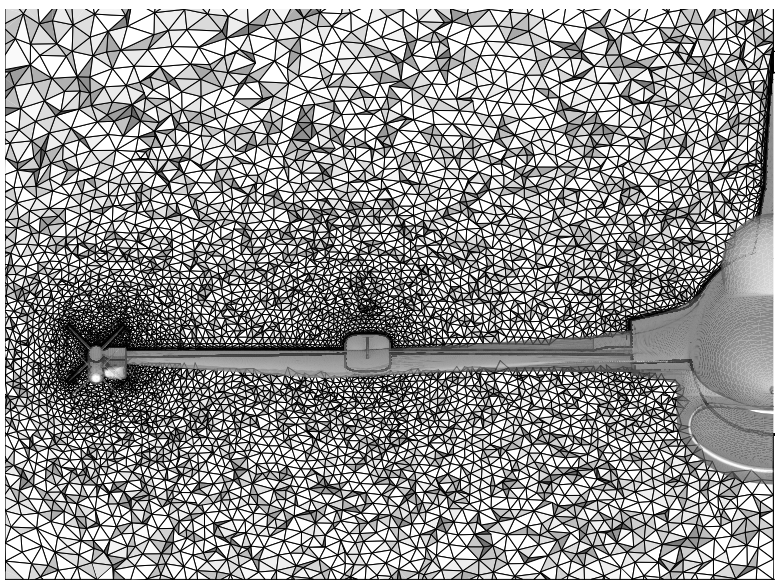

Figure 10-3: Wrinkly Cutting Plane at FS496 Showing the Grid Density off the Aircraft Surface close to the Trailing Edge.

Next, the hybrid grid was converted from Cobalt format to the "Flexible Format Architecture" (`FFA`) [10.31], the native `Edge` format. In this conversion step, all grid dimensions were converted from inches to meters.

Finally, the `FFA`-format grid was converted to the CFD General Notation System (CGNS) [10.32], library version 2.3. The resulting `CGNS` file was uploaded onto the Virtual Laboratory (VL) [10.33] at the NASA Langley Research Center to be used by other researchers in the CAWAPI group. The tools for converting grids

Table 10-2: Propulsion Conditions as a Function of the Flight Condition (FC).

	Inlet duct exit conditions				*Mixing plane cond.*	
FC	T_{stat} [K]	p_{stat} [Pa]	u [m/s]	Mach	T_{tot} [K]	p_{tot} [Pa]
FC07	276.7	75,842	115.7	0.347	583.3	158,579
FC19	269.9	70,327	105.4	0.320	583.3	148,237
FC25	261.1	60,122	144.7	0.447	671.7	181,332
FC46	246.4	40,334	123.2	0.390	580.6	102,042
FC70	288.3	73,429	141.6	0.416	666.7	206,843
FC50	244.5	35,577	147.3	0.470	641.4	116,866
FC51	239.8	35,784	142.8	0.460	636.7	115,418

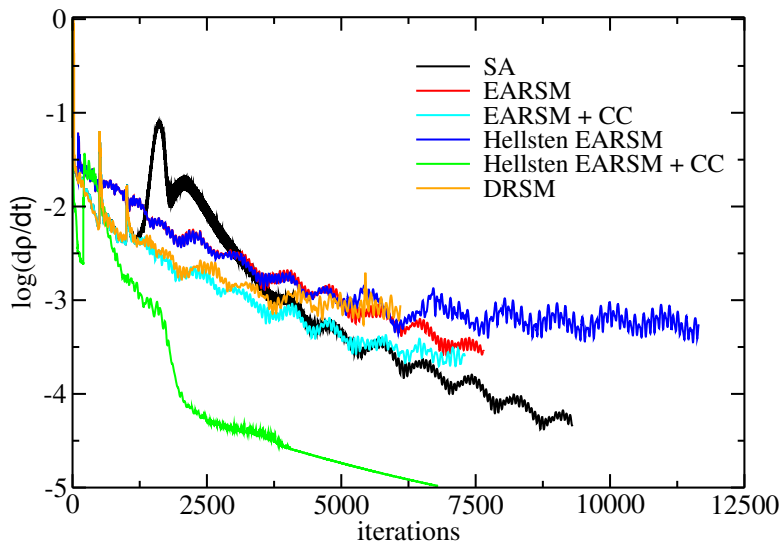

Figure 10-4: Convergence History of different RANS Turbulence Models for FC19: Density Residual versus Number of Iterations.

in `Cobalt` and `VGRIDns` format to `CGNS` format were also made available on the VL.
The boundary conditions are symmetry, adiabatic wall for the surface of the aircraft, and characteristic variable freestream conditions for the far-field boundaries, which are located about 10 aircraft length (24 root chord lengths) away from the aircraft. The boundary conditions on the inlet duct exit plane and the mixing plane are pressure outlet and total states inlet, respectively. The corresponding propulsion conditions are listed for the different flight conditions to be examined in Table 10-2. It should be noted that these conditions are generic engine conditions and do not correspond to any specific engine.
For the two flight conditions with non-zero sideslip the half-span grids were mirrored at the symmetry plane, resulting in a grid with 20,971,418 tetrahedra and 2,884,788 prisms. To investigate the influence of the number of prismatic layers on the accuracy of the results computed with the codes that require hybrid grids, a second unstructured hybrid grid with up to 20 prismatic layers was generated from the all-tetrahedral grid. This grid featured ”chopped” prismatic layers with pyramids as end caps. It was used by KTH/FOI with `Edge`.

10.7.4 Convergence

A typical convergence plot is shown for FC19 in Fig. 10-4. As the convergence criterion we used residuals of

Table 10-3: Computed Cases: Turbulence Models Used for Computing the different Flight Conditions (FC).

FC	S-A	EARSM	Hellsten	EARSM + CC	Hellsten + CC	DRSM	DES	hybrid
FC07	×	×	×	×	×	-	×	×
FC19	×	×	×	×	×	×	-	-
FC46	×	×	×	×	×	×	×	-
FC25	×	×	×	×	×	-	×	-
FC50	×	×	×	-	×	-	-	-
FC51	×	×	×	-	×	-	-	-
FC70⋆	×†	×	×	×	×	-	-	-

⋆ The wall resolution of the present grid is not sufficient for the higher Reynolds number at this flight condition.
† Calculation was performed but was unstable and no converged solution was obtained.

$\partial\rho/\partial t$ and lift coefficient history. Note that the residual dropped by more than three orders of magnitude for all turbulence models. Also note that the result for the Hellsten EARSM + CC were obtained with a newer version of the Edge code with improved convergence properties.

10.8 RESULTS AND DISCUSSION

This section contains comparisons between the CFD solutions and measured surface pressures, boundary-layer profiles and local skin friction. All mandatory and additional flight conditions have been investigated using six different turbulence closure models and DES. Table 10-3 lists the 37 different cases that have been computed. Note that the curvature corrected version of the EARSM have been considered here because the uncorrected model tends to overestimate the eddy viscosity in vortical flow. Curvature correction limits the maximum eddy viscosity in the vortex core. The steady-state solutions were computed using a second-order accurate central scheme for the mean flow equations and a second-order upwind discretization of the turbulent equations. The CFL number was set to 1.0. Convergence acceleration was achieved through local time stepping, residual smoothing and full multi-grid with three levels. Fully turbulent flow was assumed and the solutions were initialized with freestream conditions, which were computed from the flight conditions in Table 10-1 assuming the atmospheric properties of the 1976 Standard Atmosphere. The angle of attack α was set to the actual angle of attack, however, the side slip angle β was set to zero for a half-span model and to the actual angle of attack for the full-span models used for computing FC50 and FC51s.

For DES, assuming a local CFL number of one and a maximum velocity $U_{\max}$ in the LES (or focus) region equal to twice the freestream velocity, the guidelines for DES by Spalart [10.34] suggest a physical (outer) time step of $\Delta t = \Delta_0/U_{\max} \approx 2.5 \times 10^{-4}$ s, where the average cell size Δ_0 in the focus region was estimated to equal 0.05 m for the grid used here. This corresponds to a non-dimensional time step $\Delta t^* = \Delta t \cdot U_\infty/c$ of 0.0033. The inner loop CFL number was set to 1.0. The time-dependent simulations were initialized with the steady-state solution computed with the Spalart-Allmaras turbulence model. More than 10,000 outer time steps were run and time-averaged.

10.8.1 Surface Pressure Coefficient

Surface pressure coefficient data is available for all flight test conditions. Figure 10-5 shows positions of butt lines (BL) and fuselage stations (FS) where the pressure coefficient was measured.

Here we focus on three flight conditions, two at subsonic Mach numbers - one at a moderate angle of attack and one at a high angle of attack (FC46 and FC25, respectively) - and one at a transonic Mach number (FC70). All of those conditions were calculated with the Spalart-Allmaras model and two EARSM, with and without curvature corrections. In addition, DES was performed for both subsonic flight conditions. FC46 was also simulated with the DRSM.

The pressure distributions for the remaining flight conditions - FC07, FC50 and FC51 - are compared to flight-test data in the Appendix. Note that the experimental surface pressure data for FC07 (and FC19) were not available. The solutions for FC07 are therefore compared to flight test data for FC49, which is for the same nominal angle of attack and side slip angle.

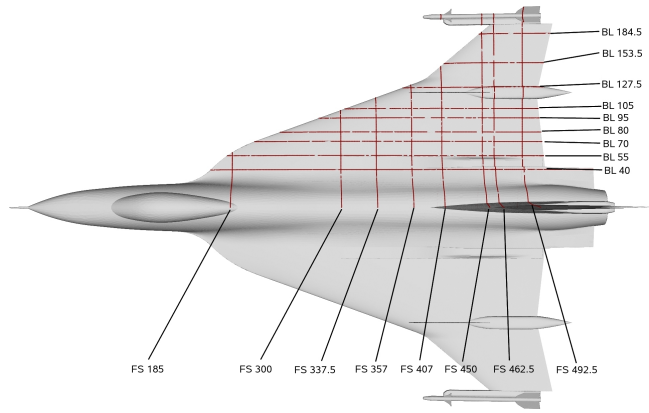

Figure 10-5: F-16XL-1 Geometry with Position of Butt Lines (BL) and Fuselage Stations (FS) where C_p Was Measured in Flight.

10.8.1.1 Flight Condition FC46

Flight condition FC46 is a condition at moderate angle of attack. The flow-field topology is shown in Fig. 10-6, which shows an iso-surface of helicity.

Figure 10-7 demonstrates that the the main C_p features, including suction peaks, are generally well predicted, both chordwise and spanwise, but not in all details. The primary suction peaks are slightly over-predicted, especially at BL 80, 95 and 105 (not shown here). The secondary suction peaks, on the other hand, are very well predicted. The chordwise location of the suction peak under the vortex outboard of the crank is predicted too far downstream/inboard (BL 153), only the DES results are somewhat closer to the leading edge. The height of the suction peak, however, is very well predicted by all models. The predictions close to the wingtip missile (BL 184.5) are rather poor, possibly due to local unsteady effects. The spread between the different turbulence models is rather significant for this BL. No firm conclusions can be made regarding the predictive capability of the different turbulence models. The Spalart-Allmaras one-equation model, however, is generally seen to predict lower and wider suction peaks than the other models and the agreement with the measured data is rather poor. The DRSM is seen to predict the highest suction peaks, followed by DES. Almost no difference can be seen between the curvature corrected and the uncorrected EARSM, but all EARSM models show a stronger secondary vortex, which displaces the primary vortex. An interesting finding is that the increasing modeling complexity of DRSM and DES did not pay off in terms of the quality of the result.

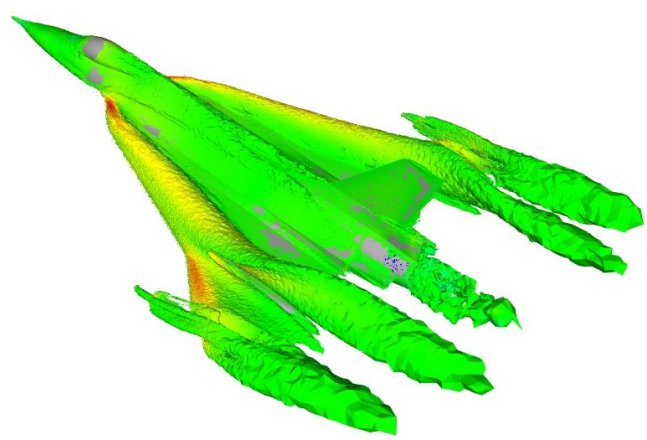

Figure 10-6: Iso-Surface of Helicity, FC46.

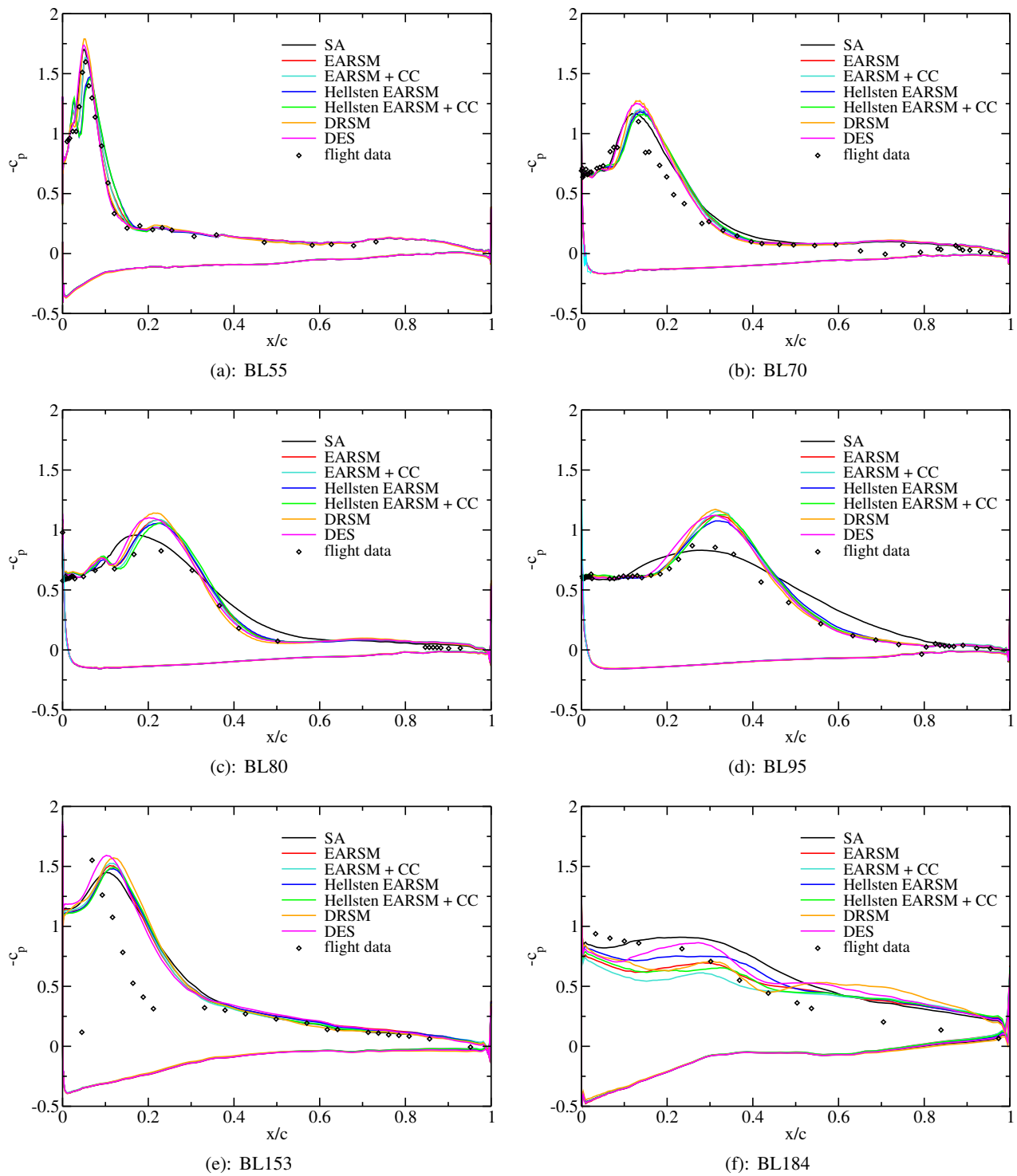

Figure 10-7: Predicted and Measured C_p Distribution at FC46.

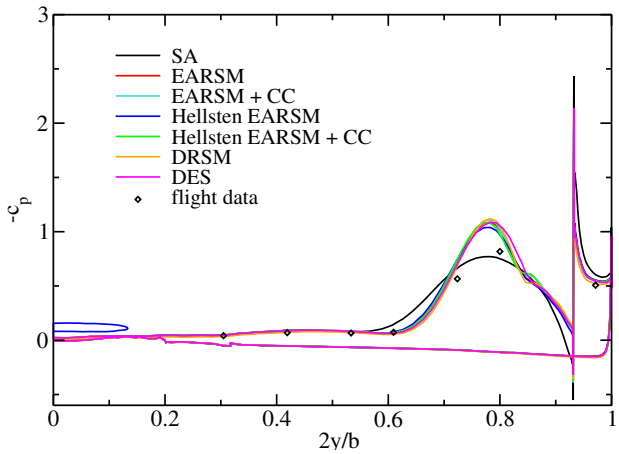

(g): FS337

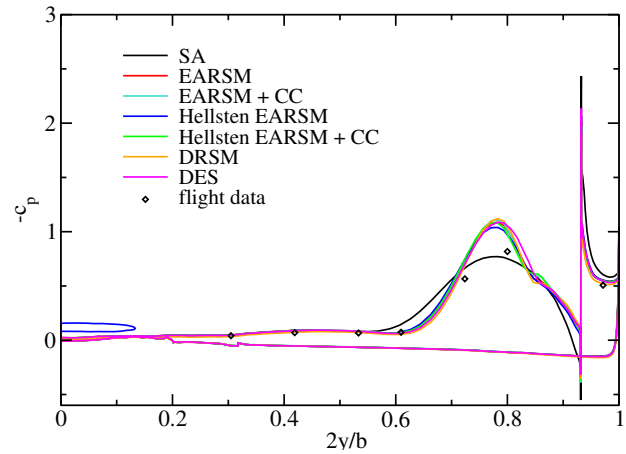

(h): FS375

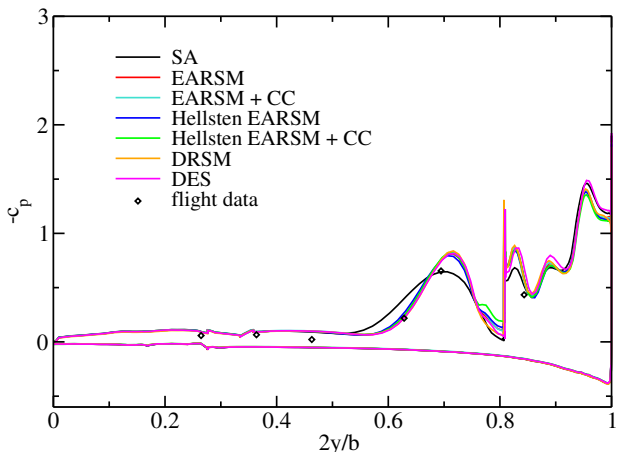

(i): FS407

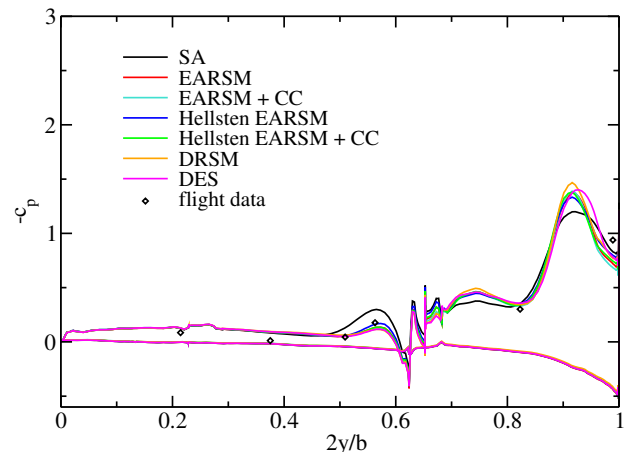

(j): FS450

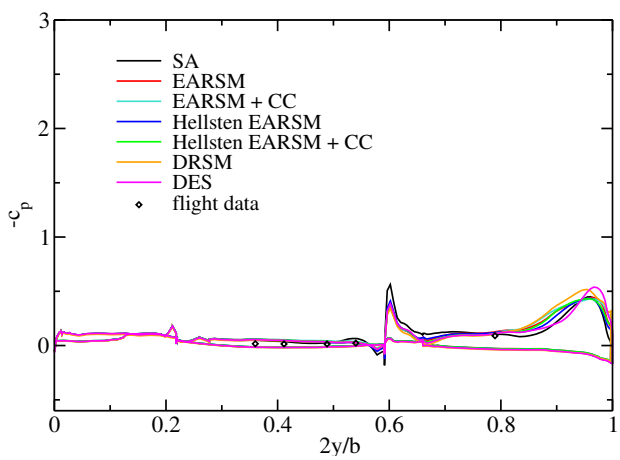

(k): FS492

Figure 10-7: Predicted and Measured C_p Distribution at FC46 (Cont.).

10.8.1.2 Flight Condition FC25

Flight condition 25 is for a higher angle of attack of 19.84°. The corresponding flow field is visualized by an iso-surface of helicity in Fig. 10-8. Comparison between flight test data and CFD is shown in Fig. 10-9. Trends which can be detected are: all model are good at predicting the primary suction peak at BL55 despite the fact that they over-predict the secondary suction peak. The S-A model departs quickly from the other models and over-predicts the primary suction peak throughout. From the family of EARSM models it is the Hellsten EARSM with curvature corrections that shows the best prediction of both primary and secondary suction peak. The only position where Hellsten EARSM + CC model shows different behavior in data compared to the flight test data is position BL 184.5. All models apart from the S-A model agree very well with the measured data at BL 153, which is outboard of the crank. None of them apart from DES predicts the C_p distribution qualitatively or quantitatively at BL 184.5, which is close to the wing tip. It turns out that the flow is separated and unsteady out there, and the higher modeling complexity of DES pays off here in predicting the correct trend in a time-averaged sense. This model is also superior over the other models when it comes to predicting the the secondary suction peak at BLs 70, 80 and 95. In addition, it is better at predicting the the span-wise position of the primary vortex, however, the magnitude of the suction peak is somewhat too low, which could be due to a displacement of the primary vortex away from the wing.

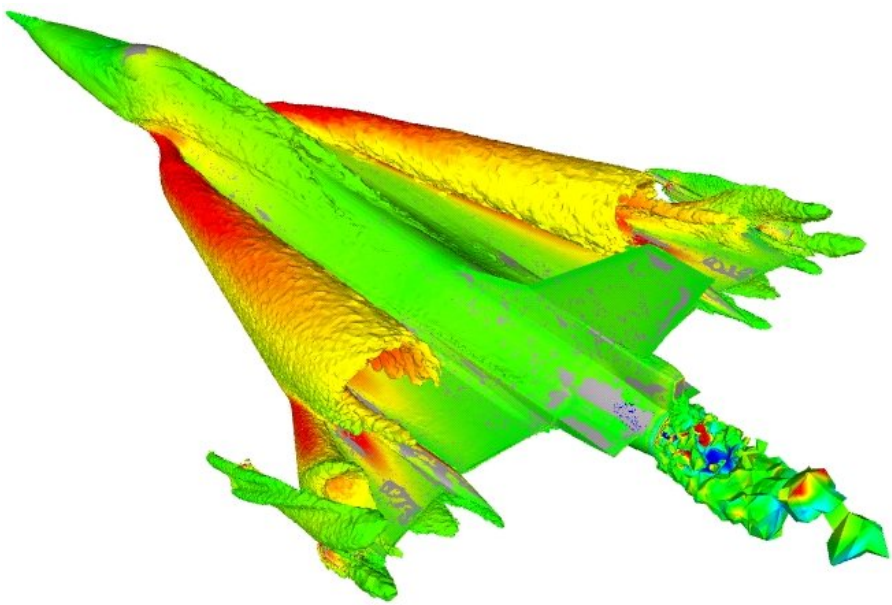

Figure 10-8: Iso-Surface of Helicity, FC25.

The unsteady nature of the vortex-dominated flow field is illustrated in Fig. 10-10, which shows a sequence of snapshots of instantaneous helicity iso-surfaces colored by C_p. The time interval between images is 5 ms and the entire sequence is over 90 ms long. Note that time increases from left to right, top to bottom. Figure 10-11 shows a time series of swirl iso-surfaces at the same intervals, which reveal that the unsteadiness is located over the rear of the wing, close to the wing tip. This explains why DES performed better than the other RANS models at BL 184.5.

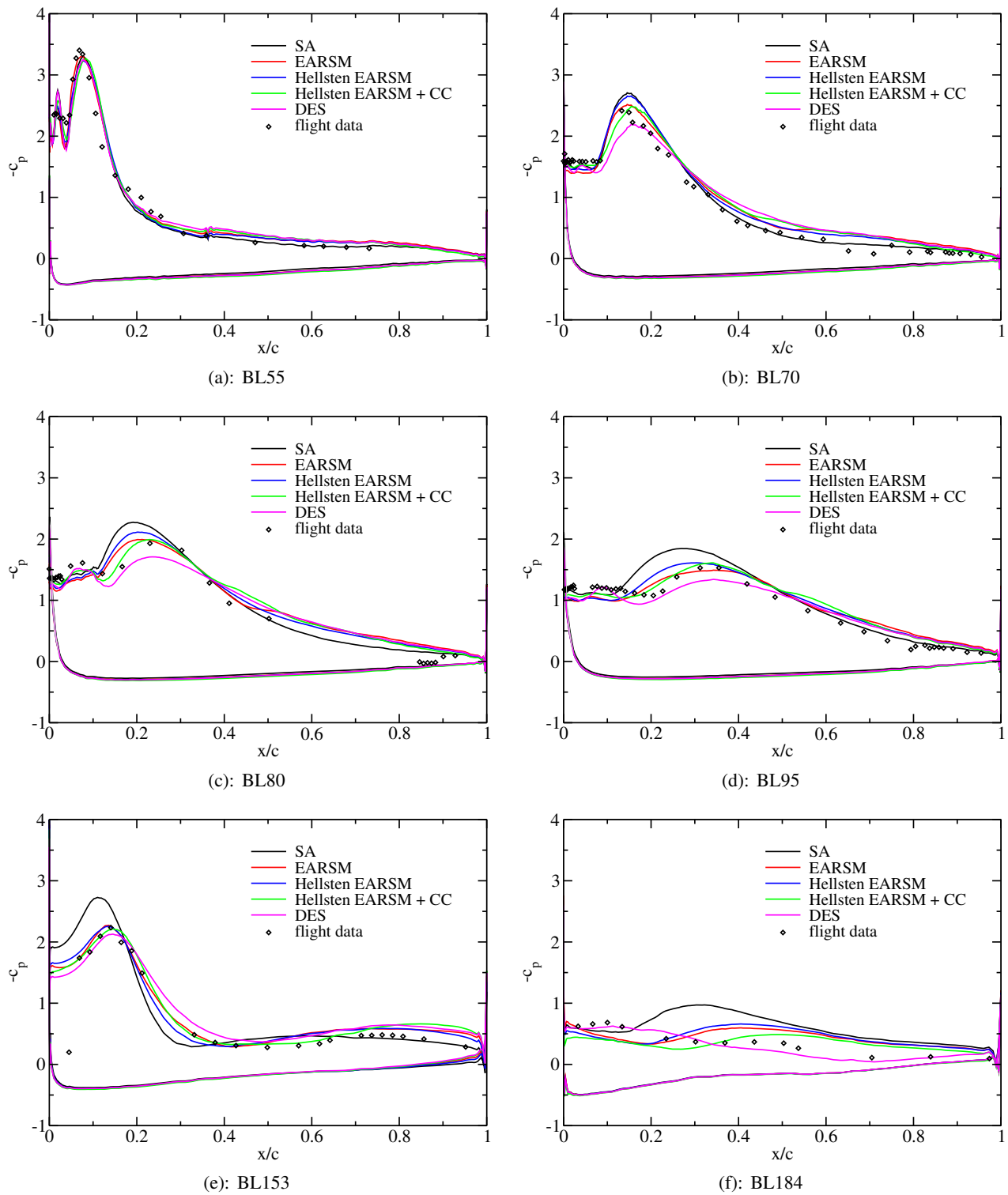

Figure 10-9: Predicted and Measured C_p Distribution at FC25.

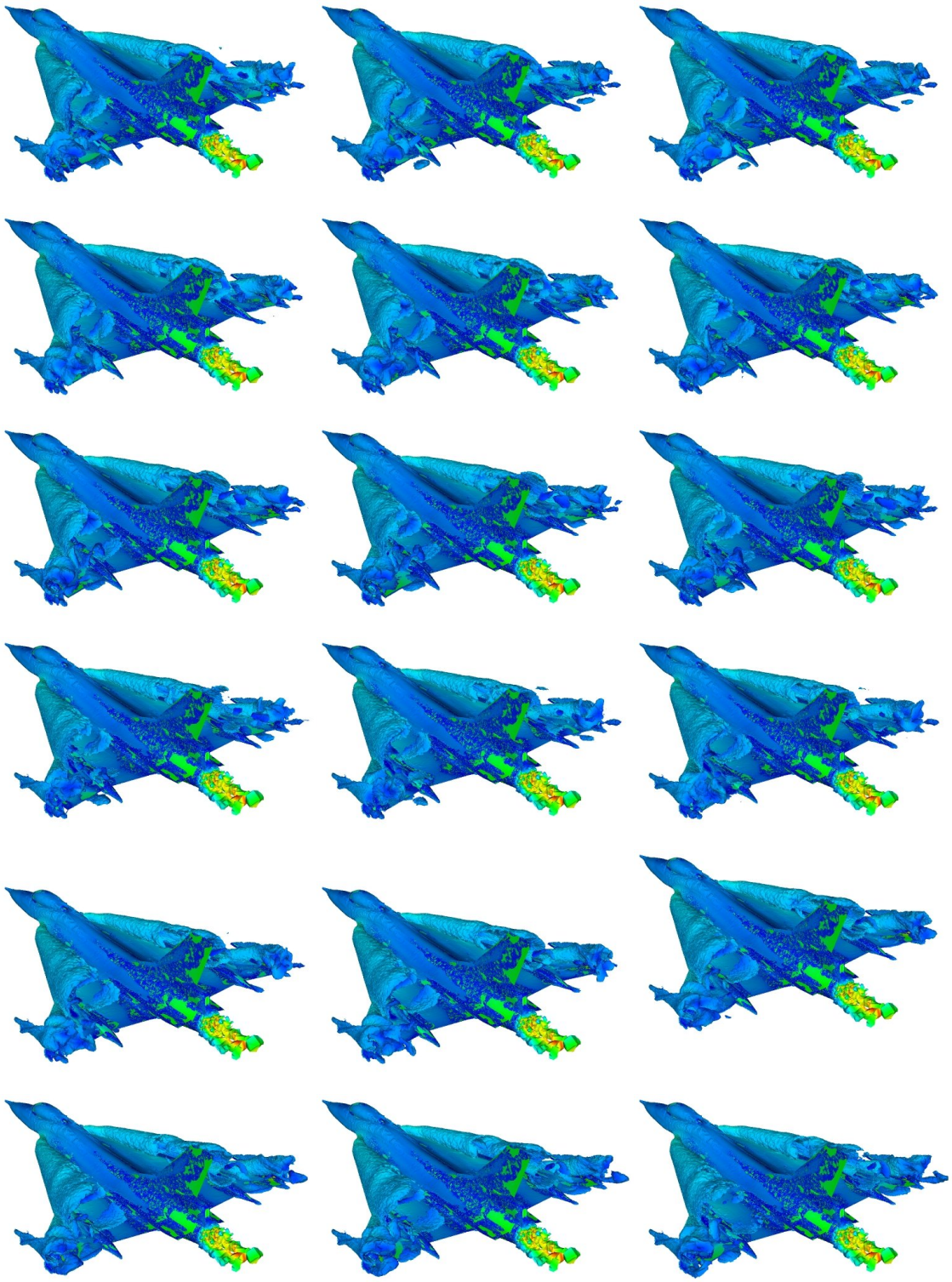

Figure 10-10: Iso-Surface of Helicity Colored by c_p, $t_1 = 0.416ms$, $\Delta t = 0.0001$, FC25.

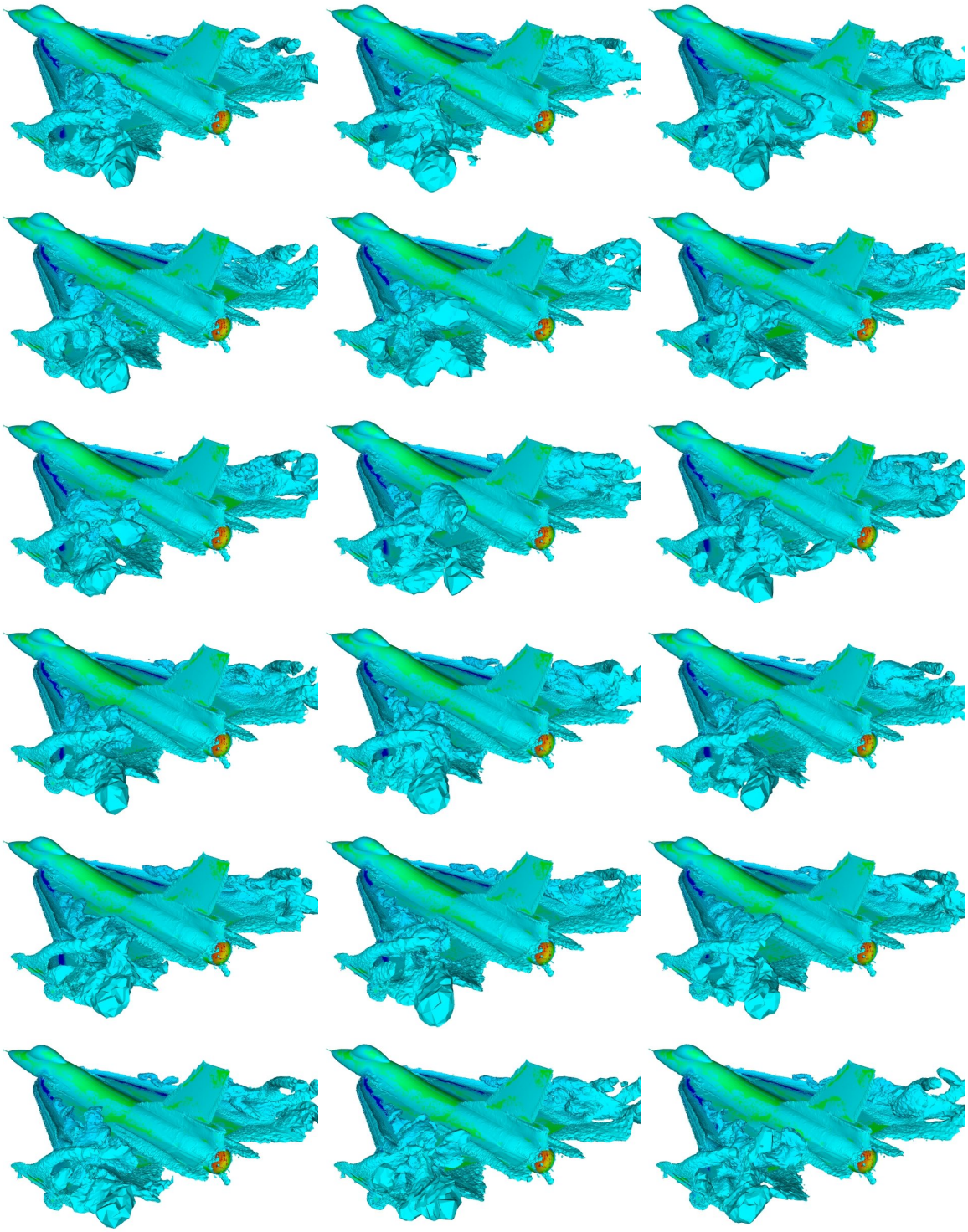

Figure 10-11: Iso-Surface of Swirl $t_1 = 0.416ms$, $\Delta t = 0.0001$, FC25.

10.8.1.3 Flight Condition FC70

Flight condition 70 corresponds to a transonic Mach number. The helicity iso-surface in Fig. 10-12(a) depicts the transonic flow field with multiple shocks. The comparison of the CFD results with flight test data is shown in Fig. 10-13.

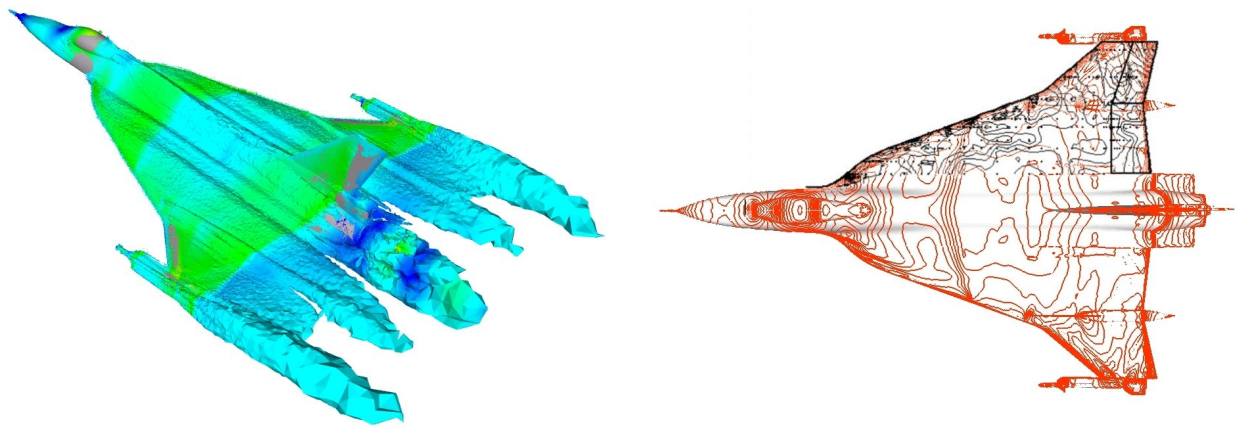

(a): Iso-Surface of Helicity, FC70.

(b): Comparison of C_p Isolines from CFD and Flight Data (Lamar et al. [10.1]), FC70.

Figure 10-12: FC70.

Interestingly, it was not possible to obtain a converged solution using the S-A model. One possible explanation for this behavior is the production of kinetic energy in the vicinity of the shock wave for different models. While standard eddy-viscosity models have a dependency of the production of kinetic energy $k \approx S_{ij}^2$, EARSM builds this relation based on $k \approx S_{ij}$. As can be noticed, all four EARSM models gave identical results. All models have fairly good predictability in BL55, BL95 and BL105 and BL127 (last two positions not included in figure) and poor predictability at BL70 and BL80 and at outboard wing. CFD predicts shock wave on the lower side of wing early BL positions fairly well.
Figure 10-12(b) shows the superposition of isolines from the CFD solution with isolines generated from flight test data [10.1]. The shock predicited by CFD is almost normal to the main flow direction. The Flight data indicates that the shock persists up to BL70, from where the flow topology is different.

This can be also seen in the C_p distribution at FS 337 (Fig. 10-14(a)). CFD predicts a flat increase of pressure along the span up to 80% of span whilst the flight data shows a pressure distribution with large variations. Figure 10-14(a) shows two peaks of high suction around 60% and 80% of span. Again, the early positions on the span show fairly good agreement of CFD and flight data meanwhile mid section of the wing show completely deffierent behaviour of picture of pressure.
At outboard wing the prediction is poor. CFD predict higher suction in the frontal part of the wing meanwhile flight data show the flow acceleration up to a shock wave which is located possibly around the hingle line of the flap. Figure 10-12(b) shows also that the pressure coefficient in parts of outboard wing reaches values of $c_p < 0.5$ which is an indicator of possible buffeting. As pointed out in [10.1] the post-flight examination of the geometry determined the deflection of leading edge flaps, elevon and ailerons. Possibly this might be a cause of discrepancies. Figure 10-14(b) shows CFD and flight data comparison at fuselage station FS 492.5 which is a located mostly on the elevon and aileron. The question is wether the lower suction predicted by the flight test is an effect of the deflection of the control surfaces.

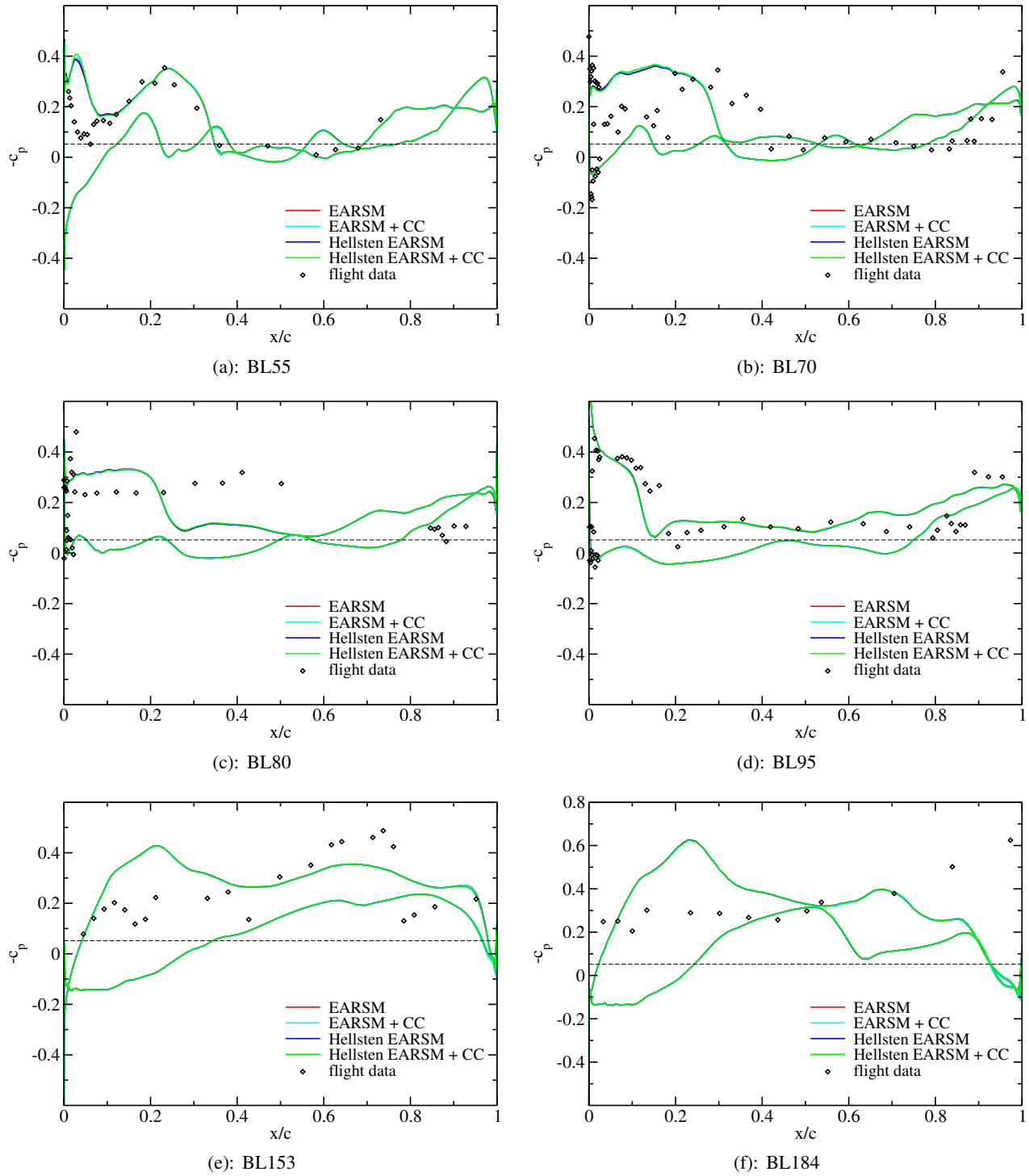

Figure 10-13: Predicted and Measured C_p Distribution for different Butt Line (BL) Stations at FC70.

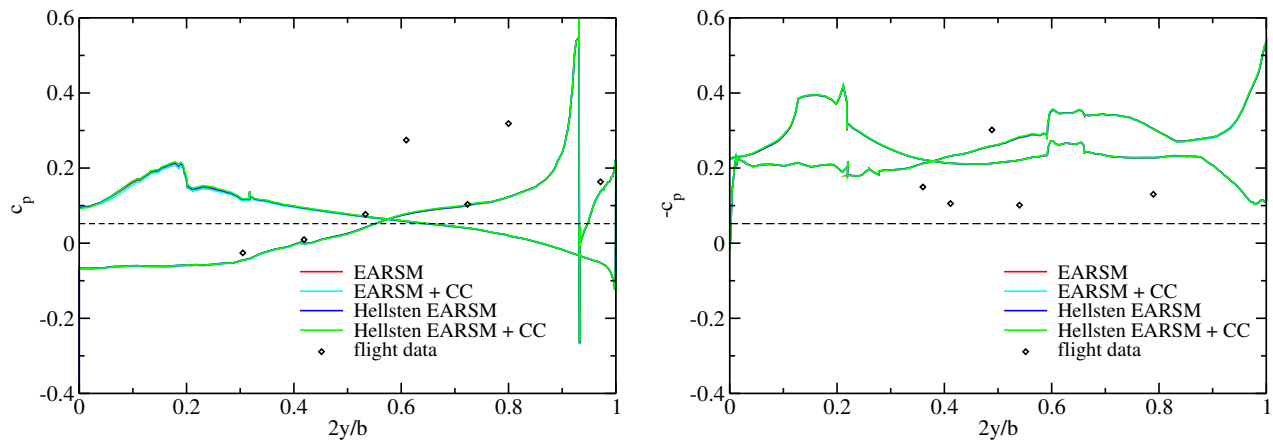

(a): FS375.5 (b): FS492.5

Figure 10-14: Predicted and Measured C_p Distribution for different Fuselage Stations (FS) at FC70.

The major cause of the differences between the CFD results for this transonic flight condition and the flight test data could be attributed to the grid density, which is not sufficient where the shock-vortex interaction takes place, as reported in the Lessons Learned chapter [10.35].

10.8.2 Skin Friction Coefficient at FC19

The local skin friction, c_f, across the left wing near FS 330 was determined with 16 modified Preston tubes in flight (the modification to each Preston tube was the integration of a static-pressure port with the total-pressure tub). The tubes were aligned with the local flow by using the same initial `CFL3D` solution at FC07 that was used to determine the rake orientations. The experimental c_f values were calculated from the pressure change between the total- and static-pressure tubes.

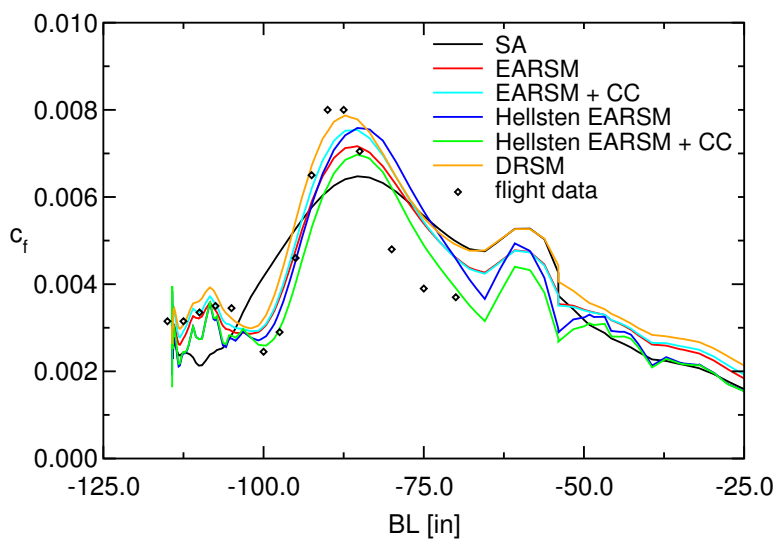

Figure 10-15: Predicted and Measured Skin Friction Coefficient for FC19 as a Function of Span at FS 330.

Figure 10-15 provides the measured and predicted c_f values at FS 330 for FC19. This figure can be used to locate and assess the impact of the vortex systems because they produce high velocities on the surface which are measured by the modified Preston tubes. Both data sets feature two regions of high c_f, which is indicative of primary and secondary vortices. Excellent qualitative and quantitative agreement is observed for both the location and absolute value of c_f under the primary and secondary/tertiary vortices. Another c_f plateaus or peak is predicted between BL 50-65, inboard of the primary vortex. It is not clear at present what this peak is due to.

Significant differences are observed in terms of the predictive capability of the different turbulence models. The results obtained with the DRSM are in best agreement with the measured c_f values. The EARSM predicts a slightly lower peak value under the primary vortex. The Spalart-Allmaras model, however, fails to predict both the peak value under the primary vortex and the region of high skin friction under the secondary vortex. Observe that the curvature correction improved the predictive capability of the the EARSM underneath the primary vortex but worsened that of the Hellsten EARSM.

10.8.3 Boundary Layer Velocity Profiles at FC07

The boundary-layer measurements were made by using two rakes at a time at four different positions on the left wing with the most inboard one used as a control. Each rake used 16 active tubes, 15 total pressure and 1 static pressure, of the 23 available. The overall height of the rakes was 2 in (5.08 cm). When mounted on the airplane, each rake was oriented into the local flow at an average angle over its height based on initial CFD predictions from the `CFL3D` code. The flow conditions were for the complete airplane (half-airplane modeled with symmetry assumed) at $\alpha = 13°$, $M_\infty = 0.29$, and $Re = 46.1 \times 10^6$, that is, FC07. The four locations were chosen as follows: one well inboard of the shed vortex systems where the flow is nearly streamwise (rake #3), one underneath the primary wing vortex (rake #4), one underneath the secondary vortex (rake #5) and one at the secondary separation line (rake #7); all are at a nominal position of FS 295 along the predicted orientation which takes into account the flow at and slightly off the surface. The average of these local flow directions was used to establish the rake orientation angles. These angles were measured from the centerline with the rake pointing forward and inboard and have values of $7.5°$, $45°$, $27.5°$, and $23.5°$, for rakes #3, #4, #7, and #5, respectively.

The processing needed to determine the velocity magnitudes for comparison with the boundary-layer rake data was not straightforward, because the velocities needed to be established along a normal to the surface at the specified points in order to be comparable with the rake data. Nevertheless, the velocity profiles were extracted from the CFD solutions at exactly the locations where the flight test data were measured using the rake probes. The first step of the extraction procedure included identifying a grid cell on the surface containing the coordinates of a probe BL/FS location. The grid nodes of this cell on the surface were then used to calculate the corresponding surface normal vector. Since the distribution of the total pressure probes was known from the rake geometry, the physical coordinates were defined using the normal vector and rake geometry data. The velocity vectors were then interpolated in `Ensight` from the surrounding mesh nodes. At each point, the magnitude of velocity as well as the three components of the velocity vector were collected. The velocity profile used for comparison with the experimental data was computed by projecting the velocity vector in the rake direction using the rake orientation angles given above.

Figure 10-16 shows the comparison of measured and predicted boundary-layer profiles for rake locations #3, #4, #7, and #5, respectively, at FC07. Underneath the primary vortex (rake #4 location), Fig.10-16 (b) shows excellent qualitative and quantitative agreement between the measured and predicted results. Both the measurements and the CFD solutions indicate a "jet-type" flow to commence for $y > 0.25$. Both results also show regions of quasi-linear variation of the velocity with y, indicative of being outside the boundary layer and just in the influence of the primary vortex. The comparison at the secondary separation line (rake #7), shown in Fig.10-16 (d), is equally good, however, it appears that the measured velocity is not asymptotic at the rake extreme; this leads to the conclusion that the maximum velocity has not been achieved at this location. Under the secondary vortex (rake #5), Fig.10-16 (c), the numerical results predict a somewhat "fuller" velocity profile, whereas the measurements suggest a slightly more retarded profile. The measured profile for rake #5, underneath the estimated location of the secondary vortex, also only achieves edge velocity near the rake

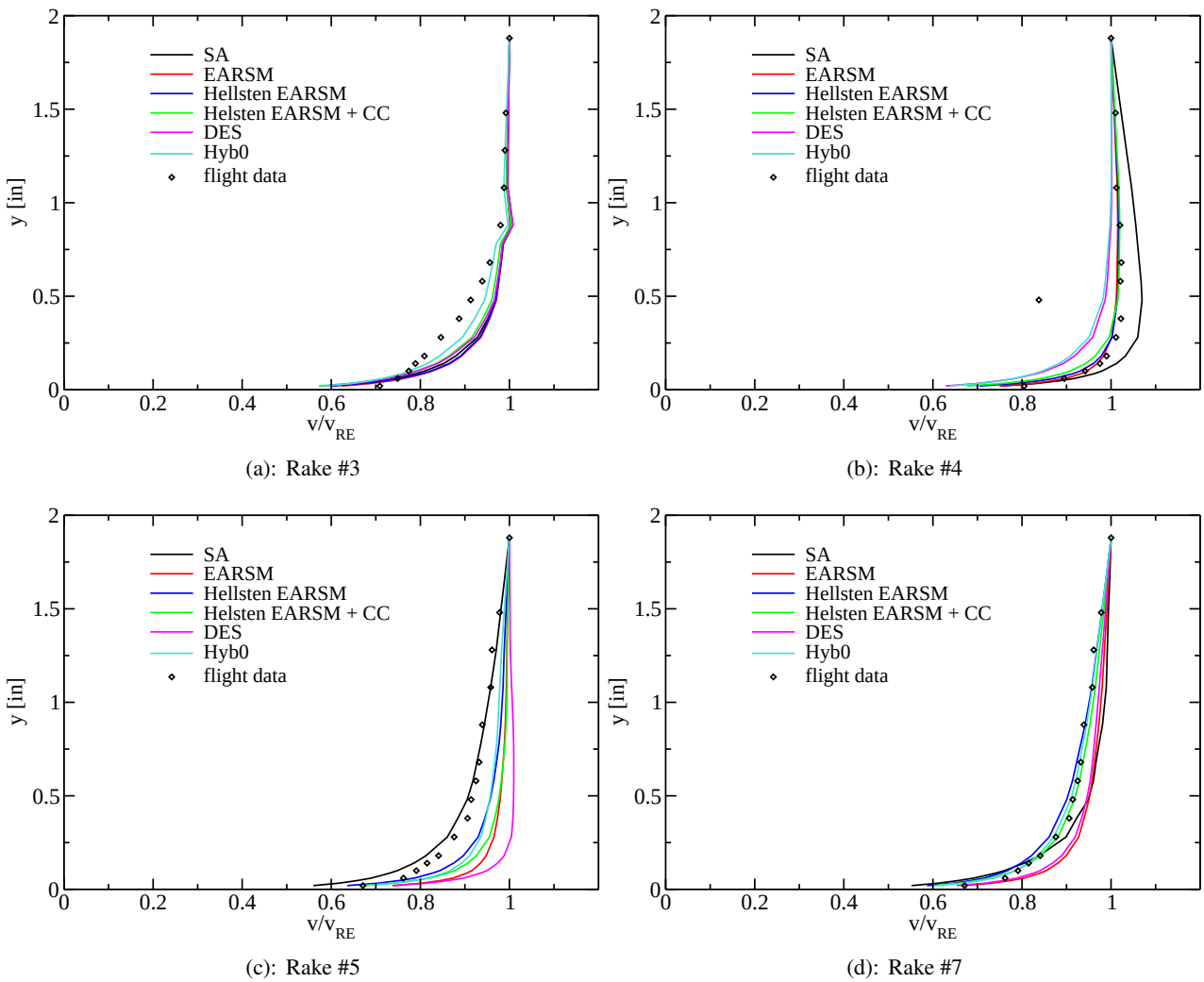

Figure 10-16: Predicted and Measured Velocity Profiles for Boundary Layer Rakes at FC07.

extreme. The quasi-linear growth of velocity for $y > 0.5$ for these profiles is associated with vortices around these boundary-layer rakes because the velocity field produced outside a representative vortex core varies as $1/r$.

Inboard of the shed vortex systems (rake #3), however, there is general disagreement between the measured and predicted values for $y < 0.8$ in, as shown in Fig. 10-16(a). The predicted values are significantly different. The numerical results predict a "fuller" velocity profile, whereas the measurements suggest a more turbulent profile. This comes somewhat as a surprise because rake #3 is located where the flow is streamwise and attached, which should be fairly easy to predict.

Generally, no major difference between the predictive capability of the different turbulence models is observed, apart from the results with the Spalart-Allmaras model, which predicts a stronger "jet-type" flow at rake location #4 and a more retarded flow at rake location #5. The EARSM + CC and the Hellsten EARSM + CC give the best overall results.

10.8.4 Adaptive Mesh Refinement at FC46

An important aspect in the simulation of vortical flows over delta-wing aircraft like the `F-16XL-1` is adaptive mesh refinement. Pirzadeh [10.36] presented a method based on a tetrahedral unstructured grid technology developed at NASA Langley Research Center with application to configurations with vortex dominated flow fields. In his method, the interior of entropy iso-surfaces are re-meshed to improve the grid resolution. The large improvement of the adapted solutions in capturing vortex flow structures over the conventional unadapted results was demonstrated by comparisons with wind tunnel data. Pirzadeh's method has been applied by Morton *et al* [10.37] to DES computations of a delta wing and an `F-18C` at high angle of attack.

A method similar to the one by Pirzadeh is applied here to refine the grid based on the solution computed for 46 with the curvature corrected EARSM, however, the mesh refinement technique used here is based on local *h*-refinement, or subdivision, rather than re-meshing. The refinement is edge-based and, depending on the number of edges marked for refinement, the tetrahedral cells are divided into two, four, or eight new cells. Here, a sensor for identifying vortices based on the ratio of total pressures [10.14,10.15] was employed to refine the grid in the vortical flow region above the wing. To determine a suitable threshold value for p_0/p_{0_∞}, the solution for FC46 was visualized in a post-processing software. Several p_0/p_{0_∞} iso-surfaces were visualized and a value of $p_0/p_{0_\infty} = 0.9$ was found most suitable to delimit the region to be refined. A minimum cells size of 0.01 m was specified to avoid refining *ad infinitum*. New nodes were not projected to the surface. The refinement procedure resulted in 685,287 new tetrahedral cells being generated. The new, refined grid is made up of a total of 11,170,996 tetrahedral elements and 1,442,664 prismatic cells, corresponding to 2,652,135 nodes. The newly generated tetrahedral elements are shown in Fig. 10-17(a). The grid was refined in the vortical flow region, capturing the primary wing vortex, parts of the secondary wing vortex, the vortex originating at the air dam and a vortex over the outer part of the wing close to the wing tip.

The grid density before and after grid refinement is shown in Fig. 10-17(b), which depicts the grid in a wrinkly cutting plane close to the trailing edge (FS496). The refinement over the wing is clearly seen in the left side of the figure. Grid cells generated due to the primary wing vortex can be discerned from cells generated due to the air dam vortex. The surface pressure distribution computed on the refined grid is shown in Fig. 10-18 for five butt line (BL) stations and on fuselage (FL) station. The refinement is seen to have almost no influence on the inboard pressure distribution and a neglige influence on the outboard pressure distribution. Actually, over the outboard wing, the suction peak underneath the primary vortex is somewhat weaker on the refined grid than on the original grid. Further refinement steps may be necessary to come to conclusive results.

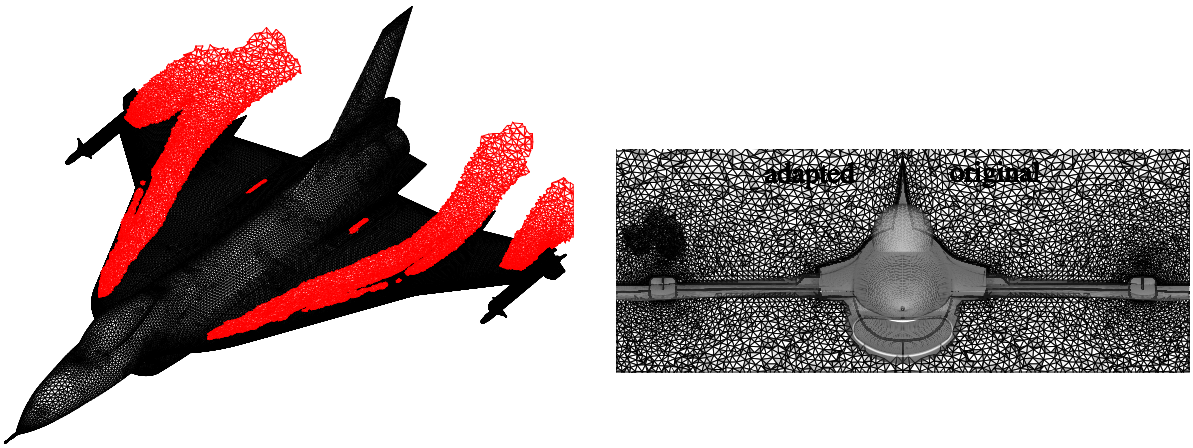

(a): **New tetrahedra (red) created by adaptive mesh refinement**

(b): **Wrinkly cutting plane at FS496 comparing the original grid (right) with the grid after adaptive mesh refinement (left)**

Figure 10-17: Solution-Adaptive Mesh Refinement at FC46.

10.9 BEST PRACTICES

The turbulent computations with the `Edge` code described above had to be sustained by changing several of the default numerical parameters, in particular the multi grid parameters.
When using the second-order accurate central scheme for the mean flow and three-level multi grid, the coarse grid dissipation coefficient, which adds 4th order dissipation on solid walls, was increased from 0.1 to 0.5. At the same time, the reduction factor for the CFL number on coarse grids was decreased from 0.8 to 0.5 and the multi-grid parameter for smoothing corrections was increased from 1.5 to 3.0. The implicit residual smoothing parameter was increased from 1.3 to 2.0 and the distance weighted residual smoothing by Mavripilis [10.38] was used instead of standard distance weighted residual smoothing.
In order to use three-level multi grid with the second-order upwind scheme for the mean flow (`minmod` limiter), the parameter for the multi-grid smoothing correction had to be increased from 1.5 to 2.0.

10.10 CONCLUSIONS

The vortical flow over a half-span, full-scale model of the `F-16XL-1` aircraft has been computed for six different flight conditions using up to six different turbulence closure models and Detached-Eddy Simulation. The CFD solutions have been compared to flight-test data for the surface pressures distribution, local skin friction and boundary layer velocity profiles.
For subsonic flight conditions the overall flow field was very well resolved. Primary, and secondary vortices inboard and outboard of the crank of the wing were captured, as well as air-dam and missile fin vortices. The only station where CFD consistently fail to predict the flight data, both quantitatively and qualitatively was the last butt line BL 184.5 where the flow is highly three-dimensional and possibly very chaotic due to proximity of AMRAAM missile.The only exception was DES which improved results at high angle of attack, however at moderate angle it does not bring any improvement. At transonic flight condition, CFD had a problem to reproduce results in the middle part of inboard wing and outboard wing. It is in contrast with rather good predictability of flight data at BL55, BL95 and BL105. At the time the cause of this is not known, it might be a

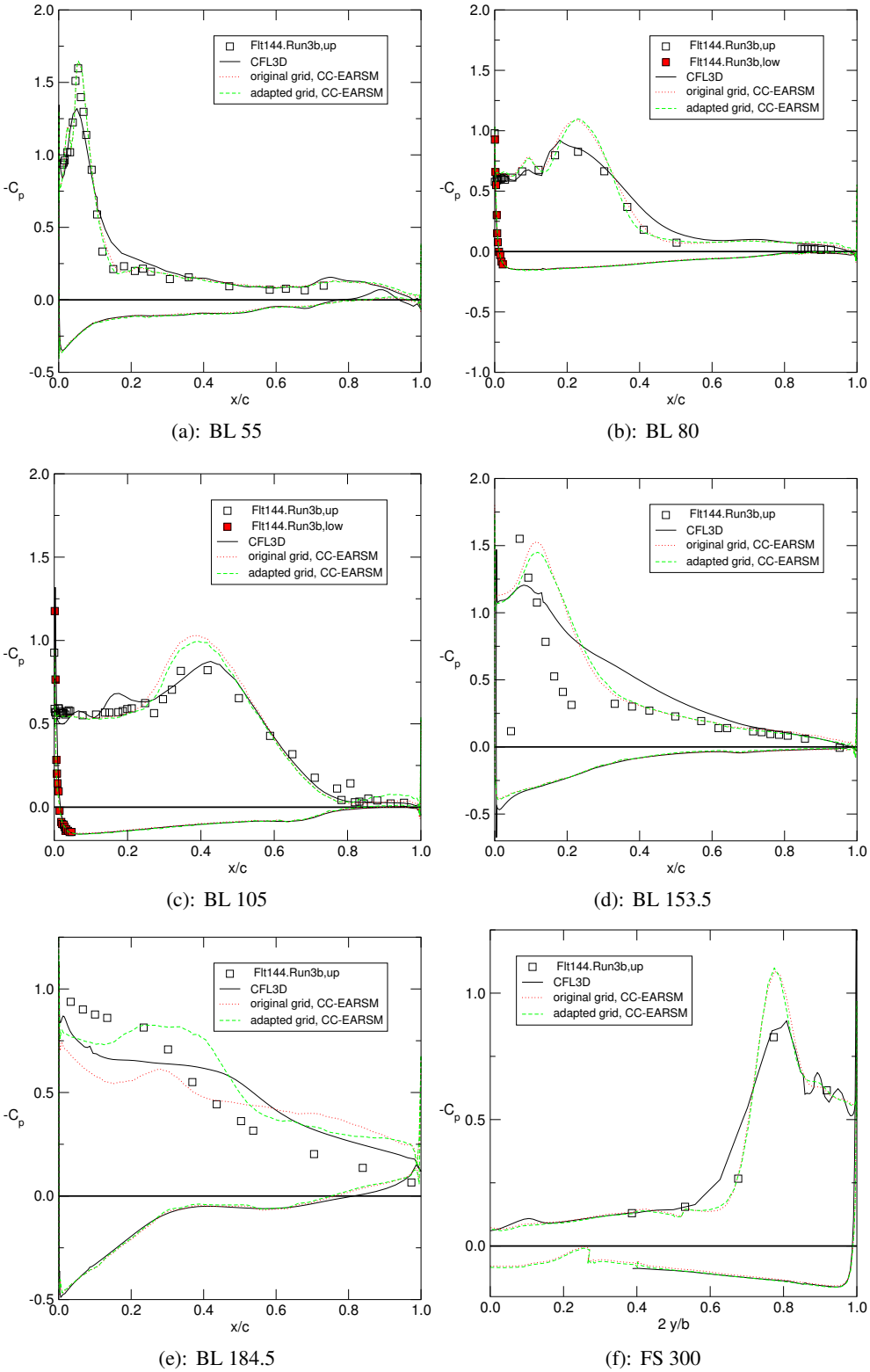

Figure 10-18: Pressure Distribution on Solution-Adapted Grid and on Original Grid Compared to Flight-Test Data at FC46.

geometrical changes such as flap, elevon and aileron deflections observed during a post-flight analysis.
Evaluating results from different turbulence models point of view it can be concluded that the S-A model is the model which had the poorest performance. Its predictability of flight data is usually very good in stations close to the fuselage and then it becomes worst. Predictability of velocity profiles was fairly good. EARSM models have usually good predictability and have consistently fairly accurate predictions of the flight data in all stations Surprisingly, the curvature corrected versions of the explicit algebraic Reynolds stress model (EARSM) did not predict better results than the uncorrected model, which is known to overestimate the eddy viscosity in vortical flows. The Differential Reynolds Stress Model (DRSM) outperformed all other models when it comes to local skin friction. DES resolved more flow features than the steady-state simulations, however, at the additional time expense. The improvement was visible at FC25 which is high angle of attack case, at moderate angles the pressure distribution from eddy-viscosity models did not differ very much from the DES solution.
None of the models is the ”very best”. The use of a particular turbulence model would be perhaps motivated mostly by confidence of user with the particular model and consistency of its results at different flight conditions rather then its performance at one flight condition. From this point of view, the recommended turbulence model for these types of flow would be Hellsten EARSM for lower angle of attack and Hellsten EARSM + CC for higher angles of attack.

10.11 ACKNOWLEDGMENTS

PDC, the Center for Parallel Computers at KTH, and NSC, the Swedish National Supercomputing Center at Linköping University, provided the resources to run most of the mandatory numerical calculations. The second author would like to acknowledge the Swedish Ministry of Defence for financial support of this project. We are also indebted to Yann Le Moigne and Lars Tysell, FOI, for helping us with the adaptive mesh refinement. Shia-Hui Peng of FOI contributed to the paper with valuable comments on DES and revisions of section B. - Turbulence modeling in Edge. The other members and guests of the NATO RTO AVT-113 task group are acknowledged for useful discussions. The authors gratefully acknowledge the support provided by the Lockheed Martin Aeronautics Company - Fort Worth in providing a refined `IGES` geometry file and the parameter values of a generic engine that were subsequently used by facet members in their CFD studies, and the geometrical work performed by Mr. Edward B. Parlette of Vigyan, Inc. in generating a series of unstructured, tetrahedral grids from the `IGES` file, with the last one known as the base grid.

10.12 REFERENCES

[10.1] Lamar, J. E., Obara, C. J., Fisher, B. D., and Fisher, D. F., “Flight, Wind-Tunnel, and Computational Fluid Dynamics Comparison for Cranked Arrow Wing (F-16XL-1) at Subsonic and Transonic Speeds,” NASA/TP 2001-210629, NASA, February 2001.

[10.2] NASA Langley Research Center, “Homepage for the F-16XL Highlift Project CAWAP,” http://cawap-prism.larc.nasa.gov, 2002, accessed 12/2004.

[10.3] Lamar, J. E., “Cranked Arrow Wing (F-16XL-1) Flight Flow Physics with CFD Predictions at Subsonic and Transonic Speeds,” *NATO/RTO Applied Vehicle Technology Panel Symposium on Advanced Flow Management: Vortex Flow and High Angle of Attack*, RTO MP-69-P-44, Loen, Norway, May 7-10 2001.

[10.4] Lessard, W. B., "Subsonic Analysis of 0.04-Scale F-16XL Models Using an Unstructured Euler Code," NASA TP 3597, NASA, October 1996.

[10.5] Lamar, J. E. and Obara, C. J., "Review of Cranked-Arrow Wing Aerodynamics Project: Its International Aeronautical Community Role," AIAA Paper 2007-0487, Presented at 45th AIAA Aerospace Sciences Meeting and Exhibit Reno NV January 8-11 2007, 2007.

[10.6] Hillaker, H. J., "F-16XL Flight Test Program Overview," *AIAA Paper 83-2730*, 1983.

[10.7] Talty, P. K. and Caughlin, D. J., "F-16XL Demonstrates New Capabilities in Flight Test at Edwards Airforce Base," *Journal of Aircraft*, Vol. 25, No. 3, 1988, pp. 206–215.

[10.8] Brower, J. N. and Scott, S. R., "The F-16XL Flight Test Program," *Society of Flight Test Engineers 15th Annual Symposium*, August 1984, pp. 9–1–9–5.

[10.9] Hahne, D. E., "Low-Speed Aerodynamic Data for an 0.18-Scale Model of an F-16XL With Various Leading-Edge Modificiations," NASA/TM 1999-209703, NASA, 1999.

[10.10] Grafton, S. B. and Nguyen, L. T., "Wind-Tunnel Free-Flight Investigation of a Model of a Cranked Arrow-Wing Fighter Configuraton," NASA TP 2410, NASA, March 1985.

[10.11] Schoonover, Jr., W. E. and Finley, D. B., "Design and Wind-Tunnel Evaluation of Vortex Flaps for the F-16XL," NASA TP 3106, NASA, October 1991.

[10.12] Eliasson, P., "EDGE, a Navier-Stokes solver for unstructured grids," *Proc. To Finite Volumes for Complex Applications III*, 2002, pp. 527–534.

[10.13] Jamason, A., "Time dependent calculations using multigrid, with application to unsteady flows past airfoils and wings," *AIAA Paper 91-1596*, 1991.

[10.14] Le Moigne, Y., "Adaptive Mesh Refinement and Simulations of Unsteady Delta-Wing Aerodynamics," *European Congress on Computational Methods in Applied Sciences and Engineering (ECCOMAS 2004)*, 2004.

[10.15] Le Moigne, Y., *Adaptive Mesh Refinement and Unsteady CFD Simulations of Delta Wings*, Ph.D. thesis, Royal Institute of Technology (KTH), Department of Aeronautical and Vehicle Engineering, Stockholm, Sweden, 2004.

[10.16] Peng, S.-H., "Hybrid RANS-LES modeling based on zero- and one-equation models for turbulent flow simulation," *Proc. 4th International Symposium on Turbulence and Shear Flow Phenomena*, Vol.3, Williamsburg, VA, USA, 27-29 June 2005, pp. 1159–1164.

[10.17] Peng, S.-H., "Algebraic Hybrid RANS-LES Modelling Applied to Incompressible and Compressible Turbulent Flows," *AIAA Paper 2006-3910*, 2006.

[10.18] Spalart, P. R. and Allmaras, S. R., "A One-Equation Turbulence Model for Aerodynamic Flows," *AIAA Paper 92-0439*, 1992.

[10.19] Wallin, S. and Johansson, A., "A Complete Explicit Algebraic Reynolds Stress Model for Incompressible and Compressible Turbulent Flows," *Journal of Fluid Mechanics*, Vol. 403, 2000, pp. 89–132.

[10.20] Wilcox, D. C., "Reassessment of the scale-determining equation for advanced turbulence models," *AIAA Journal*, Vol. 26, No. 11, 1988, pp. 1299–1310.

[10.21] Hellsten, A. K., "New Advanced k-ω Turbulence Model for High-Lift Aerodynamics," *AIAA Journal*, Vol. 3, No. 9, 2005, pp. 1857–1869.

[10.22] Wallin, S. and Johansson, A. V., "Modelling streamline curvature effects in explicit algebraic Reynolds stress turbulence models," *Int. J. Heat and Fluid Flow*, Vol. 23, No. 5, 2002, pp. 721–730.

[10.23] Hanjalic, K., Jakirlic, S., and Hadzig, I., "Computation of oscillating turbulent flows at transitional Re-numbers," *Turbulent Shear Flows 9*, 1995, pp. 323–342, Springer Verlag.

[10.24] Spalart, P. R., Jou, W.-H., Strelets, M., and Allmaras, S. R., "Comments on the Feasibility of LES for Wings, and on a Hybrid RANS/LES Approach," *Advances in DNS/LES,* 1st *AFOSR Int. Conf. on DNS/LES*, August 1997.

[10.25] Peng, S.-H., "Detached eddy simulation for turbulent compressible flows using the EDGE solver," FOI Scientific report, to be published, 2006.

[10.26] Peng, S.-H., "Simulation of turbulent flows past a rectangular open cavity using DES and Unsteady RANS," AIAA Paper 2006-2827, 2006.

[10.27] Morton, S. A., Forsythe, J. R., Squires, K. D., and Wurtzler, K. E., "Assessment of Unstructured Grids for Detached-Eddy Simulation of High Reynolds Number Separated Flows," *Proceedings of the* 8th *International Conference on Grid Generation in Computational Field Simulations*, June 2002.

[10.28] Samareh, S., "GridTool: A Surface Modeling and Grid Generation Tool," *Proceedings of the Workshop on Surface Modeling, Grid Generation, and Related Issues in CFD Solutions*, NASA CP-3291, May 9-11 1995.

[10.29] Pirzadeh, S., "Progress Toward A User-Oriented Unstructured Viscous Grid Generator," *AIAA 96-0031*, 1996.

[10.30] Strang, W. Z., Tomaro, R. F., and Grismer, M. J., "The Defining Methods of Cobalt: A Parallel, Implicit, Unstructured Euler/Navier-Stokes Flow Solver," *AIAA Paper 99-0786*, 1999.

[10.31] Wallin, S., "Standardized Data Format," Tech. Rep. FFAP-A-950, The Aeronautical Research Institute of Sweden (FFA), Stockholm, Sweden, 1992.

[10.32] Poinot, M., Rumsey, C. L., and Mani, M., "Impact of CGNS on CFD Workflow," *AIAA Paper 2004-2142*, 2004.

[10.33] Lamar, J. E., Cronin, C. K., and Scott, L. E., "A review of steps taken to create an international virtual laboratory at NASA Langley for aerodynamic prediction and comparison," *Progress in Aerospace Sciences*, Vol. 40, No. 3, April 2004, pp. 163–172.

[10.34] Spalart, P. R., "Young-Person's Guide to Detached-Eddy Simulation Grids," CR 2001-211032, NASA, 2001.

[10.35] Rizzi, A., O.Boelens, Jirásek, A., Lamar, J., and Badcock, K., "What was learned from the numerical investigations on the CAWAPI configuration," *Understanding and Modeling Vortical Flows to Improve the Technology Readiness Level for Military Aircraft. Summary Report of Task Group AVT-113*, NATO RTO Report RTO-TR-AVT-113, 2008.

[10.36] Pirzadeh, S., "Vortical Flow Prediction Using an Adaptive Unstructured Grid Method," *NATO/RTO Applied Vehicle Technology Panel Symposium on Advanced Flow Management: Vortex Flow and High Angle of Attack*, RTO MP-069(I)-(SYA)-13, Loen, Norway, May 7-10 2001.

[10.37] Morton, S. A., Steenman, M. B., Cummings, R. M., and Forsythe, J. R., "DES Grid Resolution Issues for Vortical Flows on a Delta Wing and and an F-18C," *AIAA Paper 2003-1103*, 2003.

[10.38] Mavriplis, D., Jameson, A., and Martinelli, L., "Multigrid solution of the Navier-Stokes equations on triangular meshes," *AIAA Paper 89-0120*, 1989.

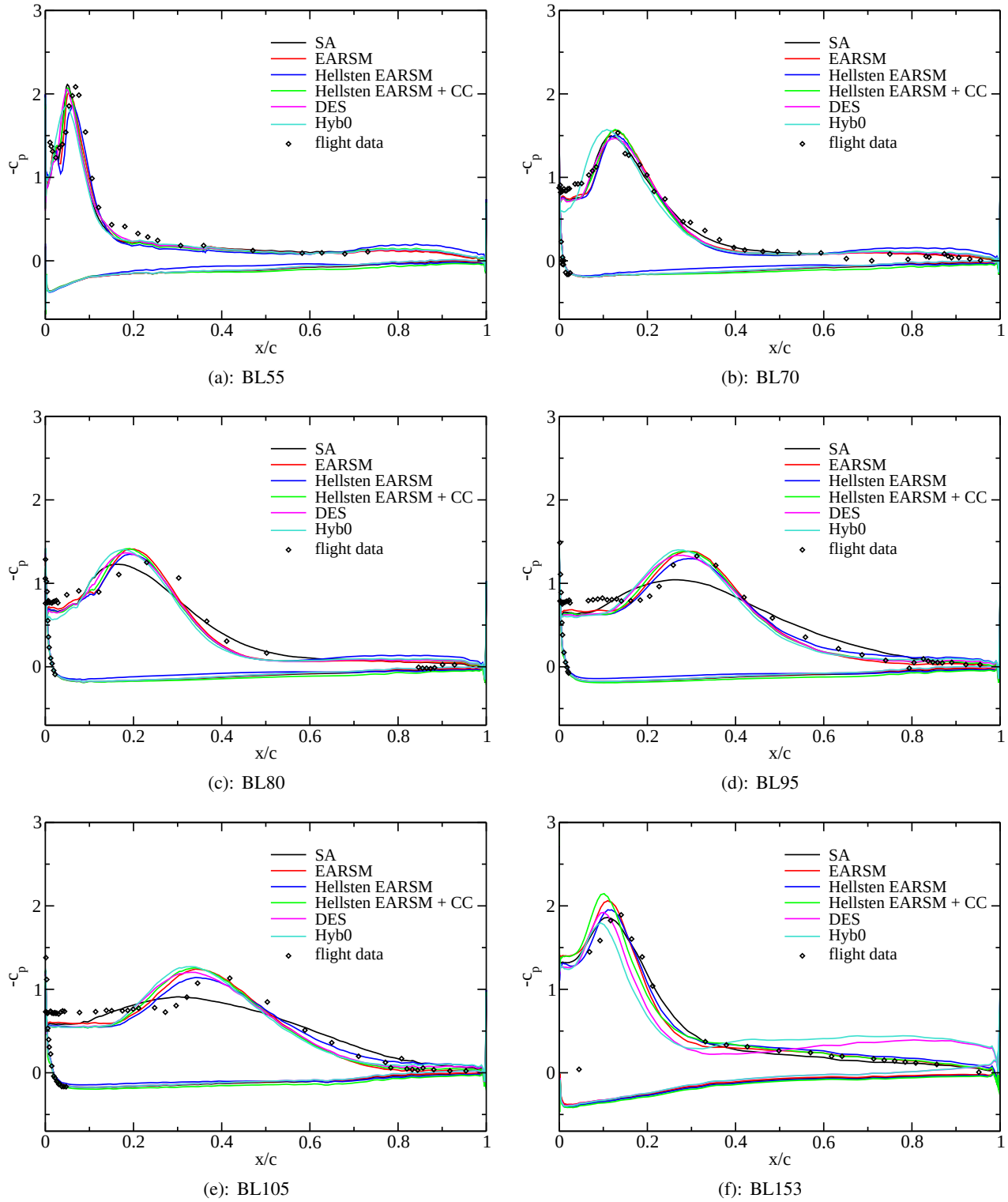

Figure 10-19: Predicted and Measured C_p Distribution at FC07.

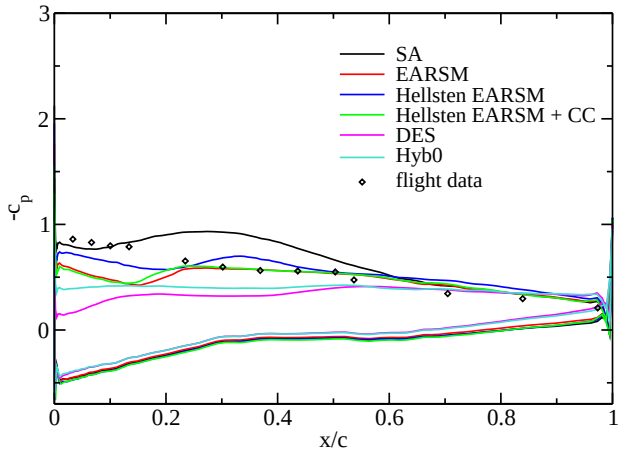

(g): BL184

Figure 10-19: Predicted and Measured C_p Distribution at FC07 (Cont.).

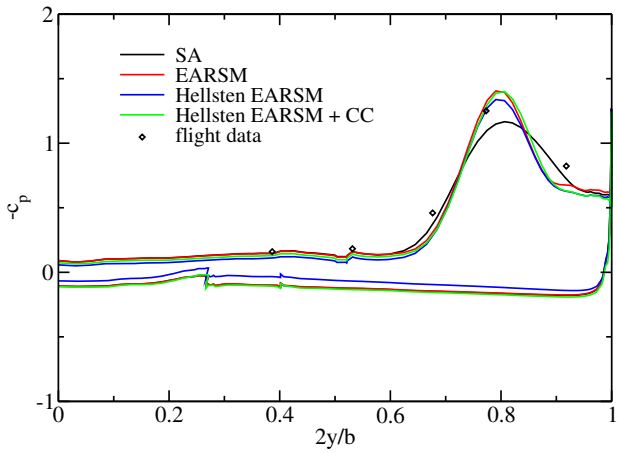

(h): FS300

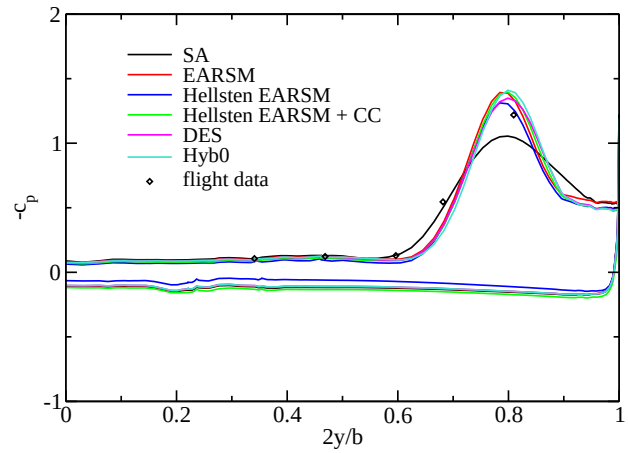

(i): FS337

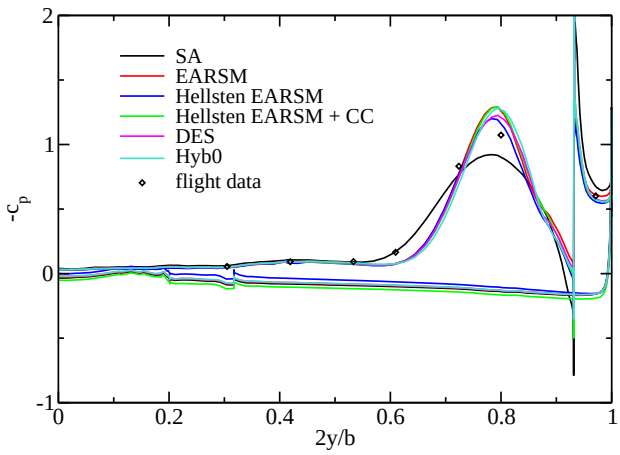

(j): FS375

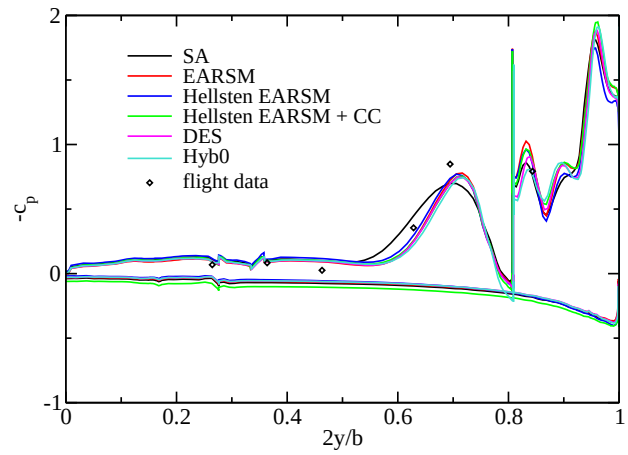

(k): FS407

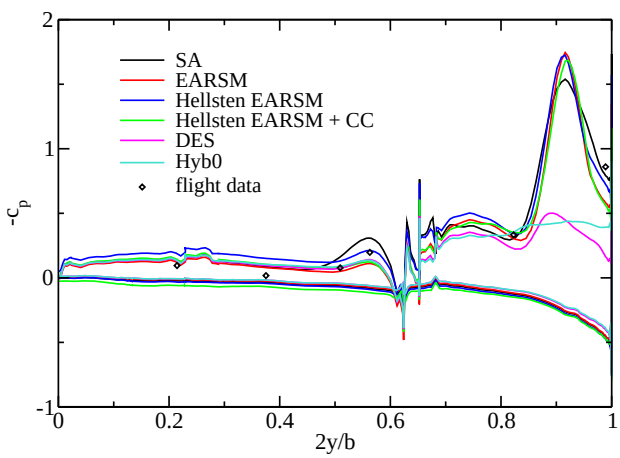

(l): FS450

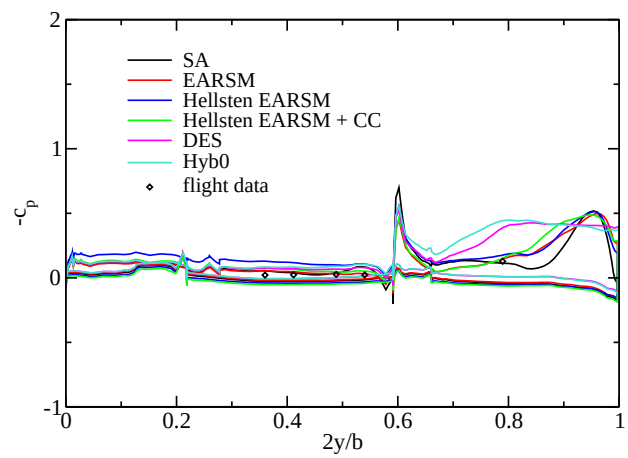

(m): FS492

Figure 10-19: Predicted and Measured C_p Distribution at FC07 (Cont.).

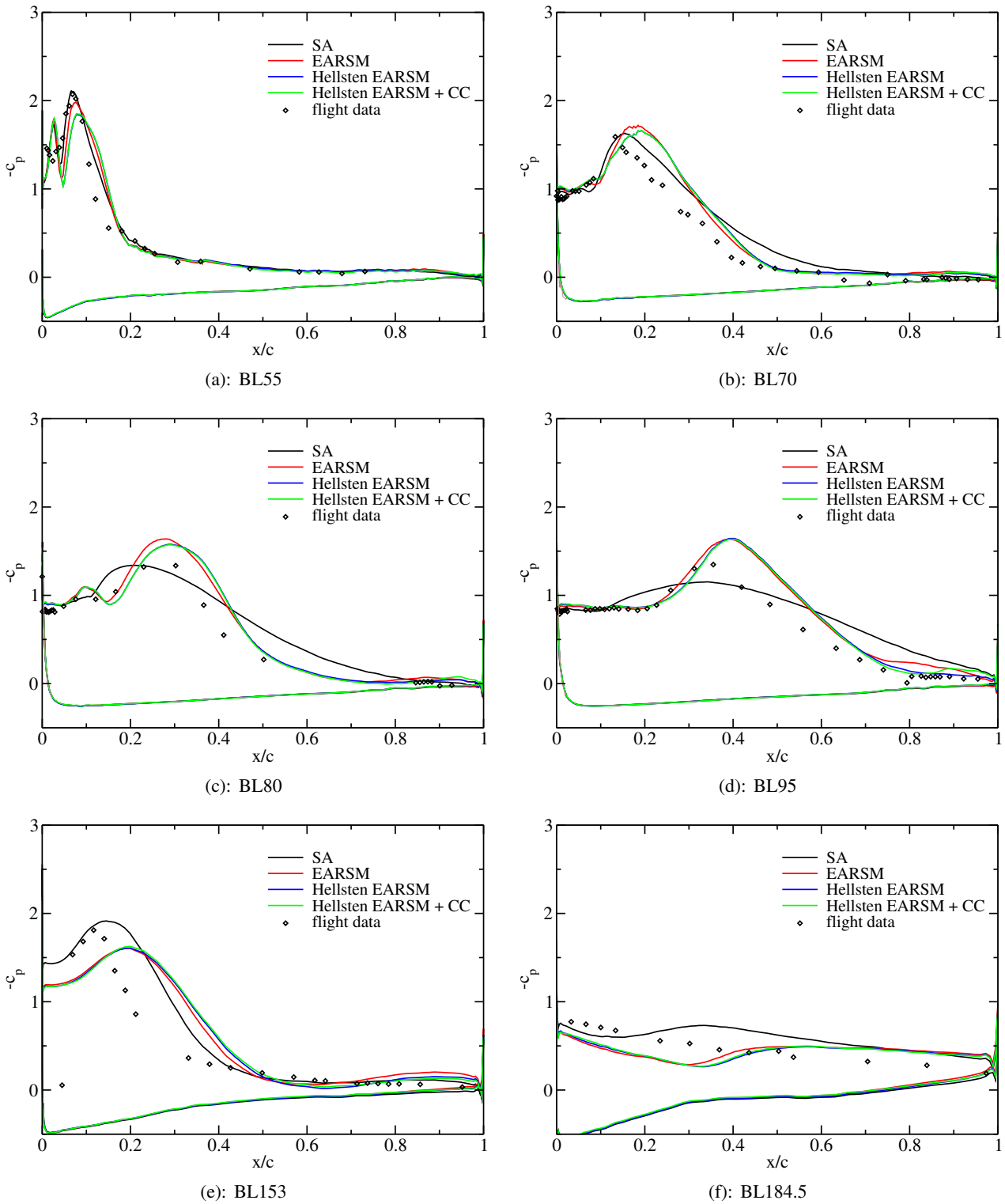

Figure 10-20: Predicted and Measured C_p Distribution at FC50.

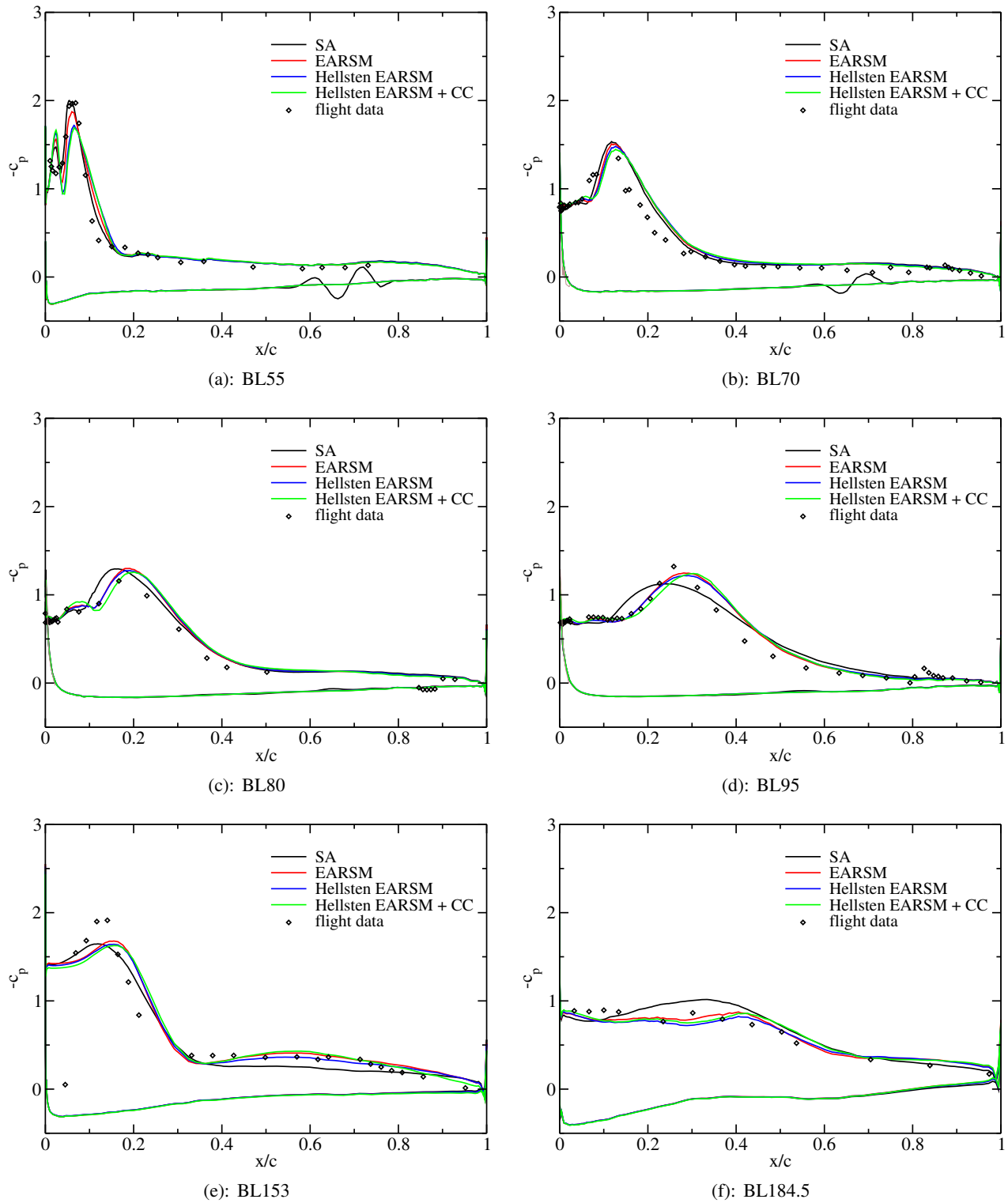

Figure 10-21: Predicted and Measured C_p Distribution at FC51.